December 2016

Computational Modeling of Transient Processes During Run-In for Tribological Systems

Rob Morien
University of Wisconsin-Milwaukee

COMPUTATIONAL MODELING OF TRANSIENT PROCESSES DURING RUN-IN FOR TRIBOLOGICAL SYSTEMS

by

Robert Morien

A Thesis Submitted in

Partial Fulfillment of the

Requirements for the Degree of

Master of Science

in Engineering

at

The University of Wisconsin-Milwaukee

December 2016

ABSTRACT

COMPUTATIONAL MODELING OF TRANSIENT PROCESSES DURING RUN-IN FOR TRIBOLOGICAL SYSTEMS

by

Robert Morien

The University of Wisconsin-Milwaukee, 2016
Under the Supervision of Professors Michael Nosonovsky and Anoop Dhingra

Understanding the frictional behavior of machine elements in mutual rolling or sliding contact is important for many engineering applications. When frictional sliding is initiated, the tribological system passes through several stages with each stage possessing its own unique frictional property. The initial transition process preceding stationary sliding is usually called "run-in". During the run-in time interval, surface topographies of frictional contacts as well as lubricant distribution and surface tribofilms reorganize and adjust through asperity deformation and wear processes before reaching the steady state. This surface stability formed during run-in leads to an improvement in frictional performance during steady state operation, which increases equipment life and efficiency. Thus, understanding of the frictional transient process and optimizing the time schedule required for the run-in of equipment such as for aircraft engines and naval vessel gas turbines can lead to improved solutions for more desirable operating conditions for the lifetime of the equipment.

This thesis investigates the running-in of both lubricated and unlubricated frictional contact in order to gain insight into how friction changes during this time interval. For lubricated

friction, it is shown that the surface topography and lubricating fluid goes through a self-organization process during run-in caused by frictional mechanisms that change the surface topography and removes fluid from the area of contact until friction and wear at the interface reaches its equilibrium value. For unlubricated friction, three common tribo-mechanical systems undergoing dry sliding during run-in are investigated: the pin-on-disk, a journal bearing, and a piston-cylinder system. Using computer simulation, a transient frictional response curve is presented for various frictional conditions in order to gain insight into how the frictional value changes during run-in. It is shown that adjustment of the static coefficient of friction can dramatically affect the response behavior with higher coefficient of friction values resulting in higher frictional forces and longer times to reach equilibrium, while smaller values shorten time to equilibrium and reduce frictional forces. These discoveries suggest seeking ways to optimize the materials in order to optimize the transient friction during run-in which are summarized in the conclusion.

Dedicated to my beautiful wife and two wonderful boys who inspire me constantly, my academic mentors who have provided unending support and guidance, and all of my family and friends who have always been a source of generosity and encouragement to me.

TABLE OF CONTENTS

LIST OF FIGURES

LIST OF TABLES

ACKNOWLEDGEMENTS

First and foremost, I would like to express sincere gratitude to my advisor Dr. Michael Nosonovsky who provided essential support and guidance imperative for successful completion of my thesis. I would also like to thank Dr. Nosonovsky for inviting me to join the Society of Tribology and Lubrication Engineers (STLE) organization and to present a research poster at one of their premier conferences in Chicago this fall semester. Appreciation and thanks are also given to Dr. Emmanuel Wornyoh who opened up his Tribology and Energy Diagnostics Lab (TEDL) to me and allowed me to operate the labs tribometer equipment. Our numerous discussions were an important source of inspiration for my decision to begin research in the field of tribology and Dr. Wornyoh's generous allowance of his time for our meetings on many late Friday afternoons must also be recognized. Additional thanks to Dr. Anoop Dhingra and Dr. Ben Church for serving on my thesis committee, kindly proofreading the entire thesis manuscript, and providing their helpful feedback.

I would like to thank all of my fellow graduate students and lab mates for their support and friendship over the past several years. I have truly appreciated working collectively on class assignments, research, and the various other organizations we have collaborated on. Last but not least I would like to thank my wife and family who backed my decision to continue my education.

1. Introduction

1.1. History of Tribology

Tribology can be found in almost all aspects of our daily lives, and with its use helps aid our efforts to complete some of our most basic tasks such as walking, gripping, or driving [1]. Tribology is defined as the science of rubbing surfaces in relative motion with one another and consists of three main categories; friction, wear, and lubrication [2]. It is of primary interest for tribologists to understand the role these three categories play within mechanical systems in order to improve working surfaces and reduce loss of energy which can lead to an improvement in equipment life and efficiency.

Friction is defined as the force which causes resistance to motion between two rubbing bodies in relative motion with one another and is generally categorized as either wet or dry [3]. Wet friction refers to contacting surfaces that have a full layer of fluid between them, whereas dry friction refers to either an absence, or partial layer of fluid between contacting surfaces. Wear is defined as loss of material due to surface asperity removal or storage when contacting surfaces rub against each other. Lubrication is the process used to help reduce friction and wear by interposing a lubricating substance between rubbing surfaces.

A large presence of friction in machinery generates adverse effects to machine components caused by frictional heating and unwanted wear. These undesirable effects caused by friction lead to a significant waste in energy and it is estimated that friction is the cause of more than one-third of the world's energy production that is wasted [4]. Thus, in order to minimize energy, tribologists seek new technologies in friction, wear, and lubrication in order to reduce waste and provide greener and more sustainable processes.

Sliding and rolling friction can be found in a wide variety of tribo-mechanical systems where power transmission is required. Examples of sliding friction include; the relative motion between a shaft and journal bearing, the piston-cylinder arrangement, or involute gears outside of the region of mesh action [5]. Rolling friction occurs when at least one of the mating surfaces is curved or wheel shaped and roll against another surface such as the cam follower, ball and roller bearings, and meshing gears inside of the region of mesh action. In order to achieve this sliding or rolling motion between two contacting bodies, the static frictional force which prevents relative motion must be overcome in order for motion to begin for either body. Once this threshold for motion has been surpassed, the system undergoes kinetic friction. Figure 1.1 illustrates this static – kinetic frictional relationship.

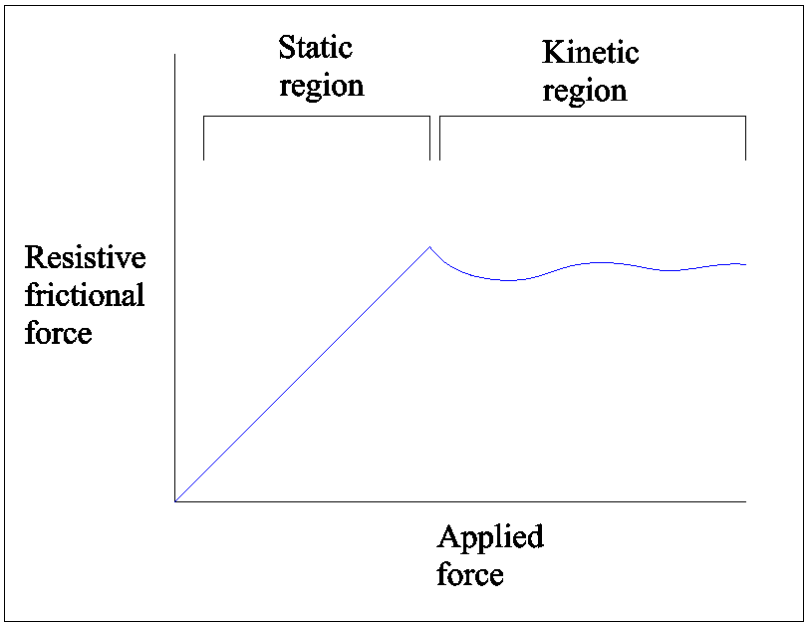

Figure 1.1, Static - Kinetic Friction Relationship

The first known quantitative investigation on friction was conducted by the polymath Leonardo da Vinci who established the first two fundamental laws for predicting frictional resistance [6, 7]. da Vinci spent nearly 20 years studying friction, lubrication, and wear and provided detailed sketches of the experiments he carried out in his renowned notebooks.

Reexamining these laws proposed by da Vinci, Guillaume Amontons articulated them into mathematical language in 1699 [8] and established a third law which we still use to this day. The first law states that the friction force is proportional and perpendicular to a normal net force which compresses the solid bodies together. If we designate the normal force by W and the friction force which always points in the direction opposite to the motion as F , the constant of proportionality, referred to as the coefficient of friction is defined as [9]:

$$\mu = \frac{F}{W} \tag{1.1}$$

The coefficient of friction is a unitless quantity which is typically established experimentally and is unique to a given pair of mating materials. Furthermore, there are two coefficient of friction values for the same pair of mating materials; one for static friction and the other for kinetic friction. Typical values used for the coefficient of friction fall into a very wide range depending on the conditions of the tribological system. This range of values can be as low as 0.0025 for rolling contact bearings and as high as 10 for clean metals in a vacuum [3, 10]. Figure 1.2 illustrates the coefficient of friction values for common materials used in industry.

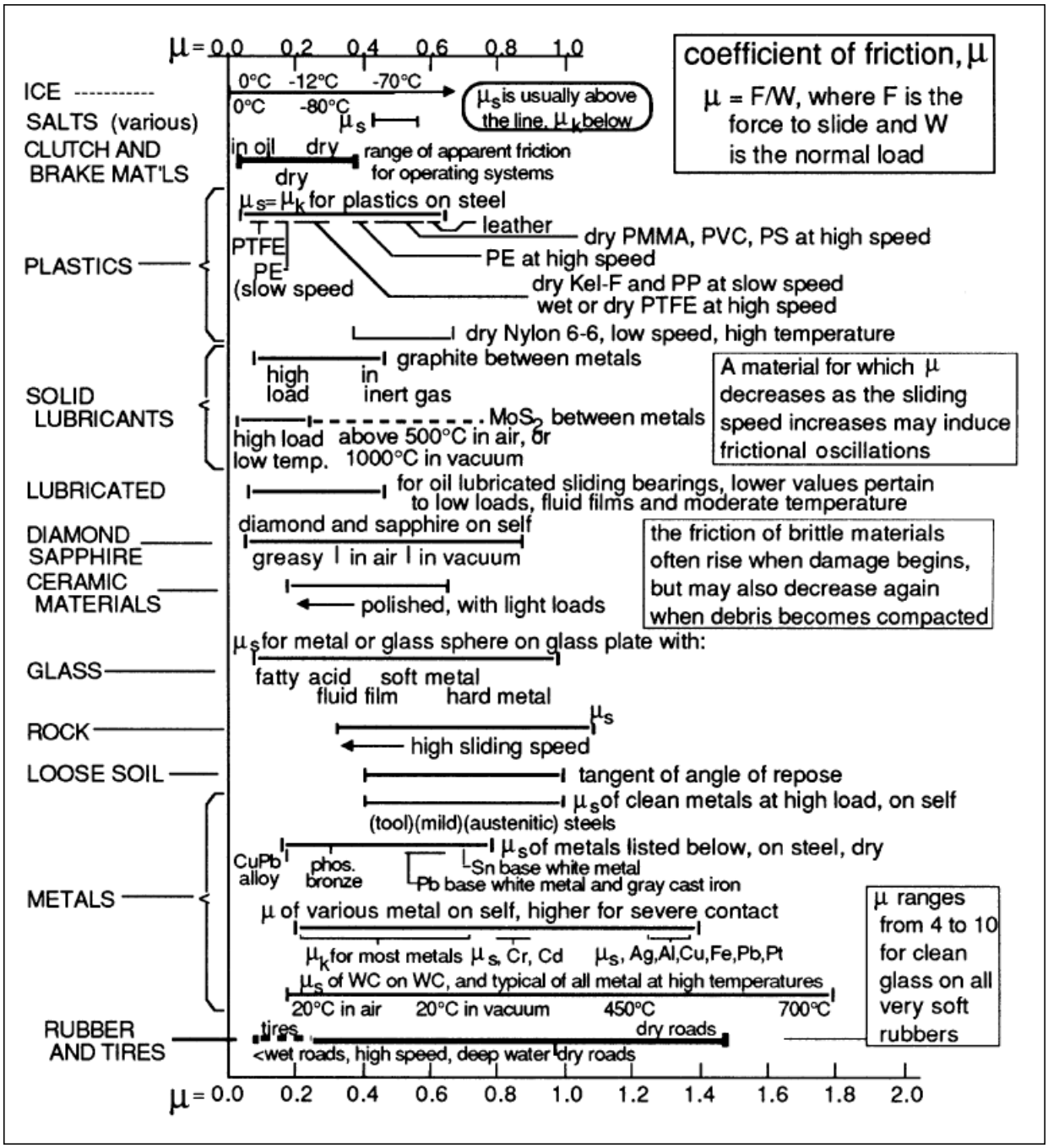

Figure 1.2, Typical Coefficient of Friction Values [11]

Although these coefficients of friction arise in several mechanical system equations, their values are generally only provided as constants and do not explain how frictional forces respond as tribological systems evolve over time. This system variance in which process variables

change with time is what is known as the transient state and in particular is generally defined as the period in time in which a tribological system advances from rest until the system reaches steady state. This period of time between rest and system settling-in is referred to as run-in.

Amontons' second law states that friction is independent of the size of the area of contact between two mating bodies. What this surprising fact states is that regardless of what side of a brick you rub against on a common surface, the friction will always remain the same. This seems counterintuitive and somewhat surprising because of the fact that the larger side of a brick will have more topography detail such as more asperities or surface roughness than the smaller side, yet still holds true under all empirical observations.

Amontons' third law, also known as Coulomb's law states that kinetic friction is independent of the speed of the contacting part. Contrary to the implications of this third law, evidence shows that often times the friction coefficient begins at a maximum value when a tribological system is at rest and changes nonlinearly as the system advances through the run-in period until it settles to a constant value as the system reaches steady state.

There have been several additional contributions to the theory of friction since the time of da Vinci leading to advancements in technology vital for the machinery used throughout the industrial revolution, drill wells used during the origins of the major oil companies, automobiles during the automotive generation, and space flight vehicles used throughout the space age.

For example, Leonard Euler showed in 1748 that if the contacting plane of two surfaces lies on an incline with an angle of α, then the coefficient of friction becomes

$$\mu = \tan\alpha \tag{1.2}$$

and, the force required to push a solid up the incline is

$$F > W \tan\alpha \tag{1.3}$$

With this inclined plane analogy for sliding motion, Euler drew a clearer distinction between static and kinetic friction and showed that kinetic friction must always be smaller than static friction since it requires more force to accelerate a mass from rest than to keep it moving.

Sir Isaac Newton also advanced the understanding of friction by providing a framework for the circular motion of fluids which he presented in the *Principia* [12], most probably the greatest scientific work of all time. In his formulations, Newton introduced the concept of viscosity, and presented Newton's law for viscous flow which states that the viscous stresses in a fluid are linearly proportional to its shear rate. Fluids that obey this law, such as gases, water, or mineral oil are known as Newtonian fluids. Newton's viscous flow theory laid the foundation for fluid-film lubrication theory.

These advances made by Euler and Newton paved the way for the industrial revolution; a period in time in which practical men started to find solutions to many of the societal problems of the day, such as the manufacturing of textiles, agricultural machinery, roads, and railways. Many improvements to bearing technology, lubricants, and lubrication also relied on the discoveries made by Euler and Newton and led to the formulation of the Navier-Stokes equations.

During this period in time, another eminent scientist, Charles-Augustin Coulomb made significant contributions to the science of tribology by both confirming the findings from previous tribologists work and extending the science to include sliding and rolling friction.

Following the industrial revolution, another major breakthrough in the science of tribology came from Richard Stribeck in which he presented a characteristic curve of the coefficient of friction plotted as a function of speed throughout the entire spectrum of motion in a tribological system. As can be seen in figure 1.3, this curve, universally known as the Stribeck

Curve, shows that friction does vary with the change in speed contrary to Coulomb's law that states that speed does not affect friction.

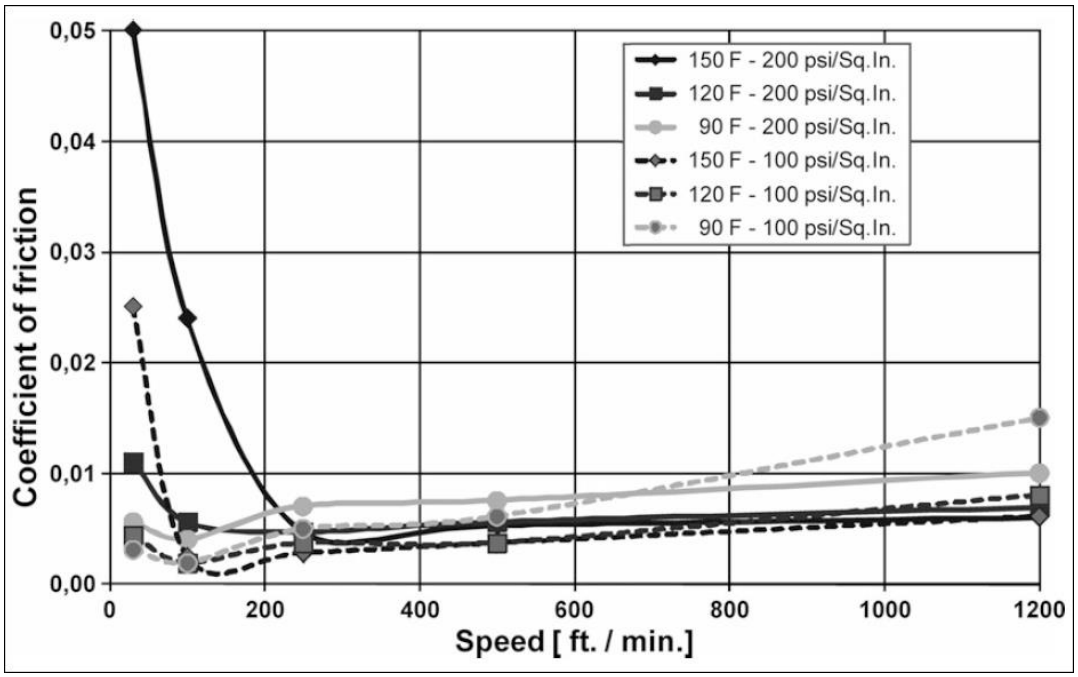

Figure 1.3, Typical Stribeck Curve [13]

The Stribeck curve is also useful for defining the four lubrication regimes found throughout a tribological system's range of motion from rest to system steady state. These lubrication regimes include; static friction, boundary lubrication, partial fluid lubrication, and full fluid lubrication and are shown in Figure 1.4.

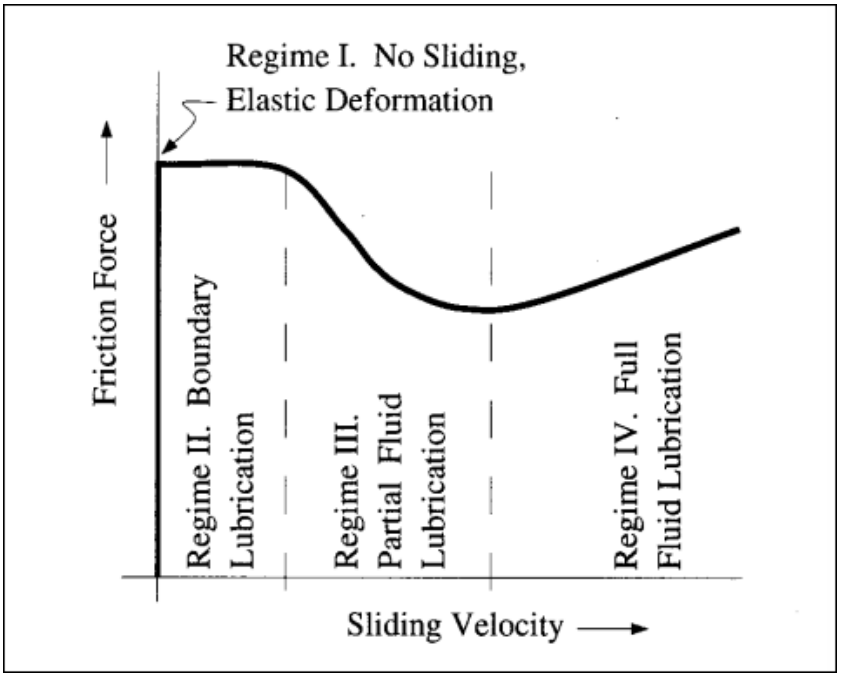

Figure 1.4, Typical Stribeck Curve Showing the Lubrication Regimes [14]

In the first lubrication regime, the static friction force prevents motion until a certain threshold is reached and break-away motion occurs. After motion is initiated, there is a transient process where the initially high coefficient of friction reduces to its stationary value. This happens because the state of the contacting surfaces changes after the sliding is initiated including their asperity roughness, and in some cases, the chemical composition of the surface layer. In the boundary lubrication regime, surface to surface contact is predominantly present with fluid just beginning to enter the interface. In this regime, full-film lubrication may not be present throughout the entire area of contact because of an increase in bearing load, a change in velocity, or insufficient lubrication supply [15]. The partial fluid lubrication regime is the intermediary between the boundary and full fluid lubrication regimes where there is a partial layer of fluid present, separating the areas of contact between the mating components. Full fluid lubrication found in the last friction regime is often referred to as the ideal lubrication condition

because of the presence of a thick film of lubrication which prevents any solid to solid contact, significantly reducing friction or wear.

In the past century, Richard Archard, another prominent scientist has advanced the science of tribology by introducing the concept of wear as the removal of abrasion particles during contact. Archards famous equation for wear states that [16]:

$$V = \frac{kWS}{3H} \tag{1.4}$$

where V is the volume of wear debris produced

k is the Archard wear constant

W is the normal load

S is the sliding distance

H is the hardness of the softest contacting surface

The aim of this thesis is to investigate three tribological systems commonly found in industrial applications by developing the theoretical and computational models which will yield a transient coefficient of friction for each system. In particular, this transient friction will be investigated for the very first couple of seconds of equipment operation. The first system that will be considered is a pin-on-disk test apparatus, the second system considered is a shaft undergoing sliding rotation inside of a journal bearing, and the third system considered is a cylinder / piston arrangement.

1.2. Objectives

The detailed objectives of the present study are:

- To develop a simplified model for tribological processes during the running-in transient state of friction in order to obtain new insights on the structure-property relationships which govern friction.
- To apply numerical simulation techniques using Maple and Solidworks commercial computational software packages for modeling friction using the above-mentioned models.
- To apply these modeling techniques to the systems of interest (a pin-on-disk test apparatus, a shaft undergoing rotational sliding inside of a journal bearing, and a cylinder / piston arrangement).
- To formulate potential recommendations for the improvement of materials and components for enhanced tribological performance such as lower friction and wear.

1.3. Method

Frictions' variance with time during the run-in period will be investigated in this thesis by beginning with a theoretical examination into hydrodynamic frictional mechanisms which affect overall system friction during the relative sliding or rolling between mating components. This system response will be modeled with a feedback loop in Maple with these frictional mechanisms entered as inputs, yielding a friction curve as a function of time.

Following the theoretical framework behind hydrodynamic effects on frictions variance with time, three tribological systems; the pin on disk test apparatus, the journal bearing, and a

piston / cylinder arrangement will be modeled and analyzed using the commercially available solid modeling computer-aided design (CAD) and computer-aided engineering (CAE) software package, Solidworks by Dassault Systèmes SolidWorks Corporation.

1.4. Thesis Organization

This chapter introduced the field of tribology where many of the important definitions were presented. Additionally, a discussion on the three fundamental laws that friction follows along with the many aspects of friction's theoretical behavior was provided.

The software and tools that are used for the computational modeling of the tribological systems in this thesis and motivations for their selection are discussed in chapter 2.

In chapter 3, a simple analytical model for fluid self-organization of lubricated contact during run-in is developed.

The first of three tribo-mechanical systems is studied in chapter 4 where we investigate pin-on-disk tribometers for measuring wear rates and frictional response. Using available experimental data, a comparison is drawn between pin-on-disk friction measurements and Finite Element Analysis (FEA). It is shown that by adjusting the friction coefficient value in the FEA, a more stabilized frictional response can be achieved during run-in.

In chapter 5, we investigate the transient frictional response of a journal bearing and shaft undergoing dry rotating contact and a comparison is drawn between available experimental data and friction measurements calculated by FEA. Using the same initial conditions in the FEA computation that were used experimentally, the transient frictional response is shown to have a large amount of action for high friction values, but by adjusting the friction coefficient value, a more stabilized response can be achieved.

In chapter 6, we investigate the transient frictional response of a piston-cylinder arrangement undergoing dry sliding contact with the geometry for the components designed using textbook information. Just as in the pin-on-disk and journal bearing systems, adjustment of the coefficient of friction results in a more stabilized frictional response.

In chapter 7, we conclude with a discussion on the transient friction results from each of the computational models followed by plans for future work in the area of tribological run-in and frictional-induced self-organization.

2. Theory and Tools Used

2.1. Introduction

In this chapter the software and tools used in this thesis to evaluate the transient frictional properties in tribological systems undergoing run-in are discussed.

2.2. Maple

Maple is a symbolic, numeric, and graphical mathematical software package developed by Waterloo Maple (Maplesoft) used for solving mathematical problems of varying complexity and provides visual representation of functions and curves through its excellent plotting capability [17]. In this thesis, Maple is used as a tool to calculate the transient response of tribological properties at the wetted contact perimeter undergoing fluid self-organization during run-in.

The power of using Maple's math engine facilitated expedient calculation of the feedback response in the tribological system which required solution of linear ODEs (ordinary differential equations) with varying input parameters. The solutions of these ODEs were then substituted back into initially derived system equations, automating the entire solution process for the final result of the transient tribological properties which are then plotted.

2.3. Solidworks and Solidworks Simulation

In chapters 4 through 6 of this thesis, finite element analysis (FEA) is used to calculate and plot the frictional transient response for three different tribological systems during run-in. 3D computer-aided design (CAD) models were developed in the Solidworks CAD modeling environment and then used for calculation of the transient friction using the Solidworks Simulation FEA package.

Solidworks is a solid modeler which enables the creation of digital models that represent actual objects in the real world [18]. During the modeling process, parametric attributes are designated such as dimensions, position, and orientation so that any changes made to an attribute parametrically updates all other features within the model. Each 3D CAD model is called a part in Solidworks and saved as a computer digital file. Parts can then be assembled together in another digital file called an assembly.

Solidworks Simulation is the general purpose FEA solver for Solidworks which is used for a wide variety of simulation computations such as static, dynamic, frequency, and vibration problems [19]. For the solutions to the transient response of friction for the three tribological systems in this thesis, non-linear analysis is used. To ensure solution convergence for non-linear type problems with an unstructured mesh, algorithm stability must be accounted for and care taken so that the CFL condition is satisfied (Courant-Friedricks-Lewy condition) [20, 21]. Since the 3D finite element mesh generated by Solidworks Simulation consists of unstructured tetrahedrals, solution stability is governed by the smallest mesh element size with the allowable time step determined by:

$$\Delta t_{CFL} = \sigma \frac{h}{a} \tag{2.1}$$

where Δt is the allowable time step, σ is a safety factor where $0 < \sigma < 1$, h is the smallest element dimension, and a is the speed of sound in the material.

The standard CAD/FEA computational software such as Solidworks, does not have an option for modeling the coefficient of friction dependency on time. However, unlike in the simple mathematical model developed in chapter 3, it is assumed in the computational models that contact occurs at a certain contact area, rather than at a point. As a result of this assumption, the effective coefficient of friction averaged throughout the entire contact area can be different

from the local coefficient of friction. This is because the shear stress is not uniformly distributed throughout the contact area. The effective coefficient of friction defined in this manner changes as a function of time, and is the reason for interest in investigating how this phenomenon affects the transient process.

3. Analytical Modeling of Transient Friction Undergoing Hydrodynamic Effects During Run-In

3.1. Introduction

During the mechanical run-in period for new equipment, surface topographies of contacting components in relative motion settle into an equilibrium value to form the final shape and fit adjustment that will last for the duration of the equipment's lifetime [22]. This self-organization of moving surfaces in contact is influenced by lubrication and material properties such as surface roughness and wear rate, yet is rarely discussed in the literature for the run-in period. Having a fundamental understanding of the coefficient of friction as a function of time throughout this mechanical run-in period can lead to an improved selection of wear materials or lubricants to help mitigate wasted energy and increase overall equipment performance.

The total frictional force for unlubricated sliding friction results from a sum of two primary mechanisms of wear; deformation and adhesion which is represented by the following mathematical model [3]:

$$F = F_{def} + F_{adh} \tag{3.1}$$

The intensity of these frictional mechanisms depends on the surface texture at the frictional interface [23]. In order to characterize surface texture, a roughness parameter; R_a is defined [24] and a functional relationship for the coefficient of friction over time caused by system feedback from deformation and adhesion effects on surface roughness is determined.

In this chapter, we expand the surface self-organization model for unlubricated surfaces during run-in which was developed by Mortazavi, Wand, and Nosonovsky [25, 26] with an ancillary model that demarcates hydrodynamic effects on friction and wear. If we characterize the wetted frictional interface containing surface asperities by a parameter called hydrodynamic

roughness R_{hyd} , a functional relationship for the coefficient of friction may be determined by two hydrodynamic frictional mechanisms; viscous erosion and capillary action. These two simultaneous frictional processes adjust the hydrodymanic roughness during run-in until its equilibrium value is reached, resulting in minimum friction and wear. The control model in figure 3.1 illustrates the two feedback loops due to the viscous erosion and capillarity frictional mechanisms.

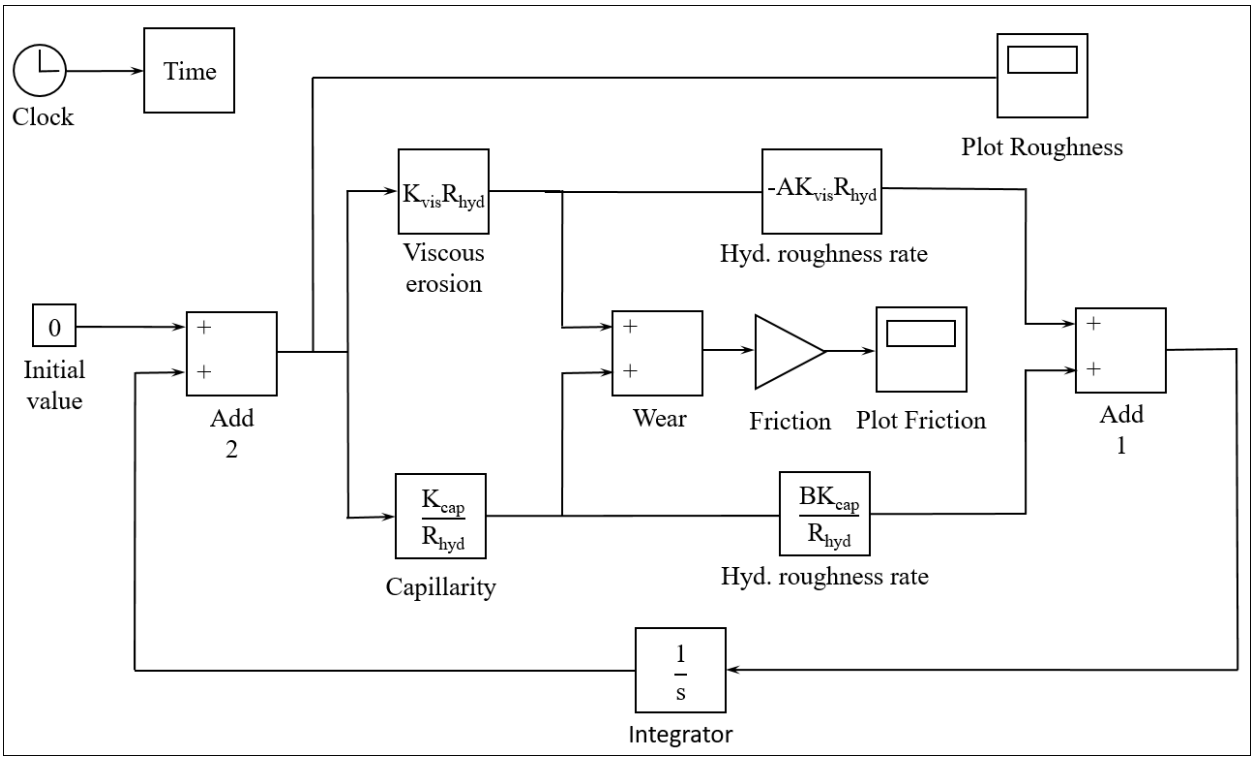

Figure 3.1, Feedback Loop Model of Two Simultaneous Frictional Mechanisms Which Combine To Bring The Hydrodynamic Roughness To Its Equilibrium Value and Minimize Friction and Wear

3.2. Fluid Self-Organization Mathematical Model

Viscous erosion and capillarity within a wetted perimeter of contacting surfaces can be perceived as two hydrodynamic frictional mechanisms which can affect friction and wear during run-in. Erosion is the process of surface wear that is caused by a fluid, stream of particles, or cavitation bubbles [27, 28]. Capillary action refers to a fluids ability to rise or fall through narrow channels such as through surface pores found on a surface with its magnitude depending on surface tension [29].

Considering first the viscous erosion frictional mechanism, higher surface asperities causes higher viscous resistance, resulting in higher friction and wear processes [30]. Therefore, a linear dependence with hydrodynamic roughness, R_{hyd} is assumed:

$$\mu_{vis} = C_{vis} R_{hyd}\,,\; k_{vis} = K_{vis} R_{hyd} \tag{3.2}$$

where C and K are proportionality constants, μ is the coefficient of friction, and k is the wear. Similar to surface roughness, R_a for dry surfaces which has units of length for surface asperity height measured by an optical profilometer at the micro scale, or an atomic force microscope at the nanoscale, hydrodynamic roughness can be determined in the same manner. Furthermore, velocity profile measurements can be used to quantify the magnitude of fluid flow resistance for fluids flowing past surface asperities and provide distinctive hydrodynamic roughness criteria for various surface roughness and fluid combinations.

The viscous erosion causes a feedback between wear and hydrodynamic roughness since surface asperities get ground down by an abrasive sanding process, creating a smoother surface. Thus, this feedback is specified as:

$$\dot{R}_{hyd} = -Ak_{vis} = -AK_{vis} R_{hyd} \tag{3.3}$$

For the capillary frictional mechanism, smoother surfaces can increase capillary effects since channel pores become narrower. Smaller capillaries tend to propel fluids higher, thus removing fluid from the wetted interface causing an increase in friction and wear. Thus, a $\frac{1}{R_{hyd}}$ non-linear dependency with hydrodynamic roughness is assumed with the following relationship:

$$\mu_{cap} = \frac{C_{cap}}{R_{hyd}}, \; k_{cap} = \frac{K_{cap}}{R_{hyd}} \tag{3.4}$$

The wear caused by capillary effects creates rougher surfaces and a feedback to the tribological system:

$$\dot{R}_{hyd} = Bk_{cap} = \frac{BK_{cap}}{R_{hyd}} \tag{3.5}$$

The constants A and B in equations 3.3 and 3.5 are phenomenological constants from thermodynamic entropy production caused by heat (friction) and mass transfer (wear) which is discussed in the dissertation by Vahid Mortazavi [31]. A combination of the viscous erosion and capillarity frictional mechanisms acting simultaneously on a wetted interface yields a net friction, wear, and rate of hydrodynamic roughness:

$$\begin{aligned} \mu &= C_{vis}R_{hyd} + \frac{C_{cap}}{R_{hyd}} \\ k &= K_{vis}R_{hyd} + \frac{K_{cap}}{R_{hyd}} \\ \dot{R}_{hyd} &= -AK_{vis}R_{hyd} + \frac{BK_{cap}}{R_{hyd}} \end{aligned} \tag{3.6}$$

As can be seen in figure 3.2, this combination of the two frictional mechanisms suggests an optimum value where a minimum coefficient of friction may be determined acting at a stationary point:

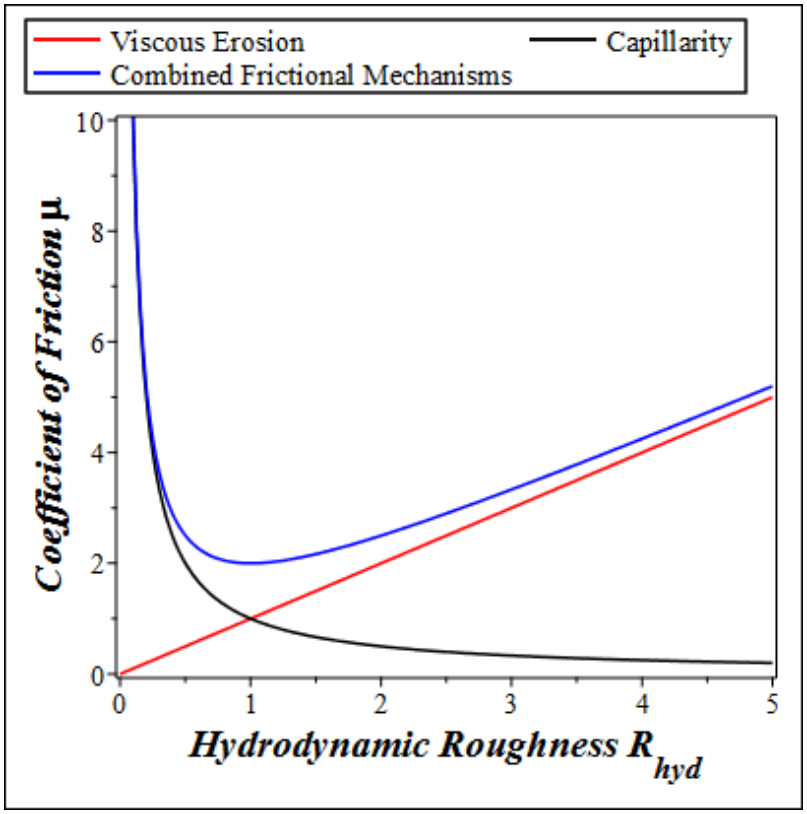

Figure 3.2, Combined Effect of Viscosity and Capillarity on Friction and Wear

In order to determine friction at the optimum value, we set the rate of hydrodynamic roughness equal to zero and solve for R_{hyd}. Therefore, from equation 3.6:

$$\dot{R}_{hyd} = 0 = -AK_{vis}R_{hyd} + \frac{BK_{cap}}{R_{hyd}} \Rightarrow AK_{vis}R^2{}_{hyd} = BK_{cap} \Rightarrow R^2{}_{hyd} = \frac{B}{A}\frac{K_{cap}}{K_{vis}}$$

Thus, the stationary point occurs at:

$$R_{hyd} = \sqrt{BK_{cap} / AK_{vis}} \tag{3.7}$$

Therefore, the coefficient of friction and wear corresponding to the stationary point becomes:

$$\begin{aligned} \mu &= C_{vis}\sqrt{BK_{cap} / AK_{vis}} + \frac{C_{cap}}{\sqrt{BK_{cap} / AK_{vis}}} \\ k &= K_{vis}\sqrt{BK_{cap} / AK_{vis}} + \frac{K_{cap}}{\sqrt{BK_{cap} / AK_{vis}}} \end{aligned} \tag{3.8}$$

The minimum wear in equation 3.6 occurs at the stationary point of k, i.e. $\frac{d}{dR_{hyd}}k = 0$:

$$\frac{d}{dR_{hyd}}k = 0 = \frac{d}{dR_{hyd}}\left(K_{vis}R_{hyd} + \frac{K_{cap}}{R_{hyd}} \right) \Rightarrow$$

$$K_{vis} = \frac{K_{cap}}{R^2_{hyd}} \Rightarrow$$

$$R_{hyd} = \sqrt{K_{cap} / K_{vis}} \tag{3.9}$$

Similarly, the minimum coefficient of friction in equation 3.6 occurs at the stationary point of μ, i.e. $\frac{d}{dR_{hyd}}\mu = 0$:

$$\frac{d}{dR_{hyd}}\mu = 0 = \frac{d}{dR_{hyd}}\left(C_{vis}R_{hyd} + \frac{C_{cap}}{R_{hyd}} \right) \Rightarrow$$

$$C_{vis} = \frac{C_{cap}}{R^2_{hyd}} \Rightarrow$$

$$R_{hyd} = \sqrt{C_{cap} / C_{vis}} \tag{3.10}$$

Therefore, minimum wear occurs at the stationary point of equation 3.7 when $A = B$. This result corresponds to a minimum coefficient of friction if $K_{cap} / K_{vis} = C_{cap} / C_{vis}$.

3.3. Results

The transient coefficient of friction and rate of hydrodynamic roughness during run-in is modeled using Maple with two feedback loops due to the viscous erosion and capillarity frictional mechanisms and their response plots are shown in figures 3.3 and 3.4.

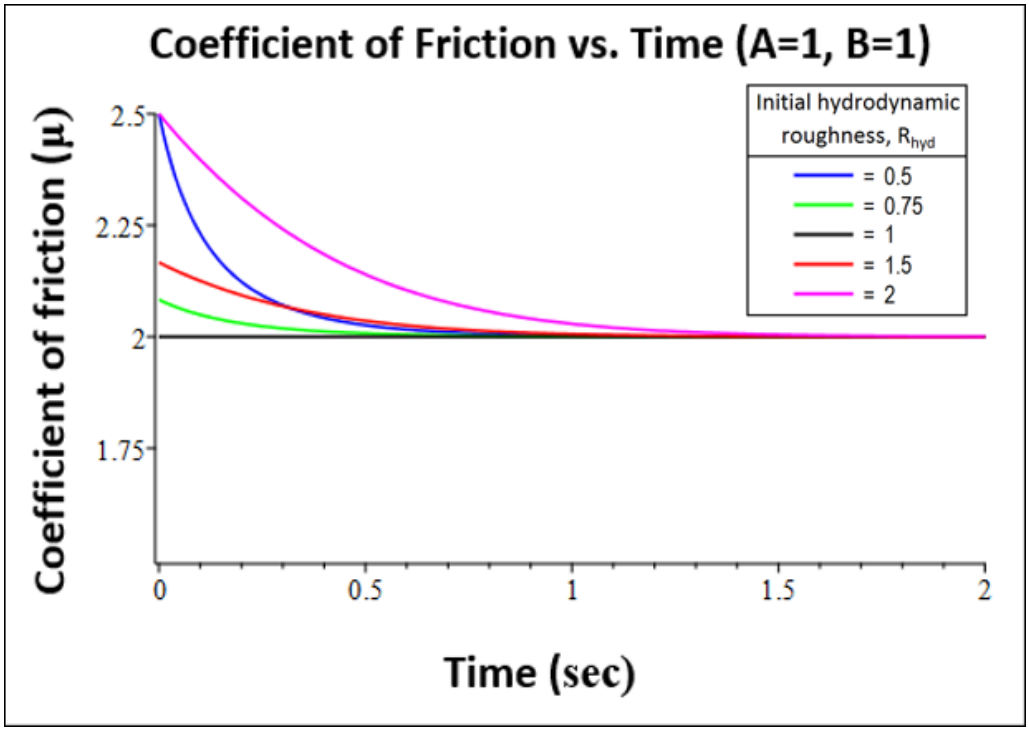

Figure 3.3, Coefficient of Friction Vs. Time during the run-in period

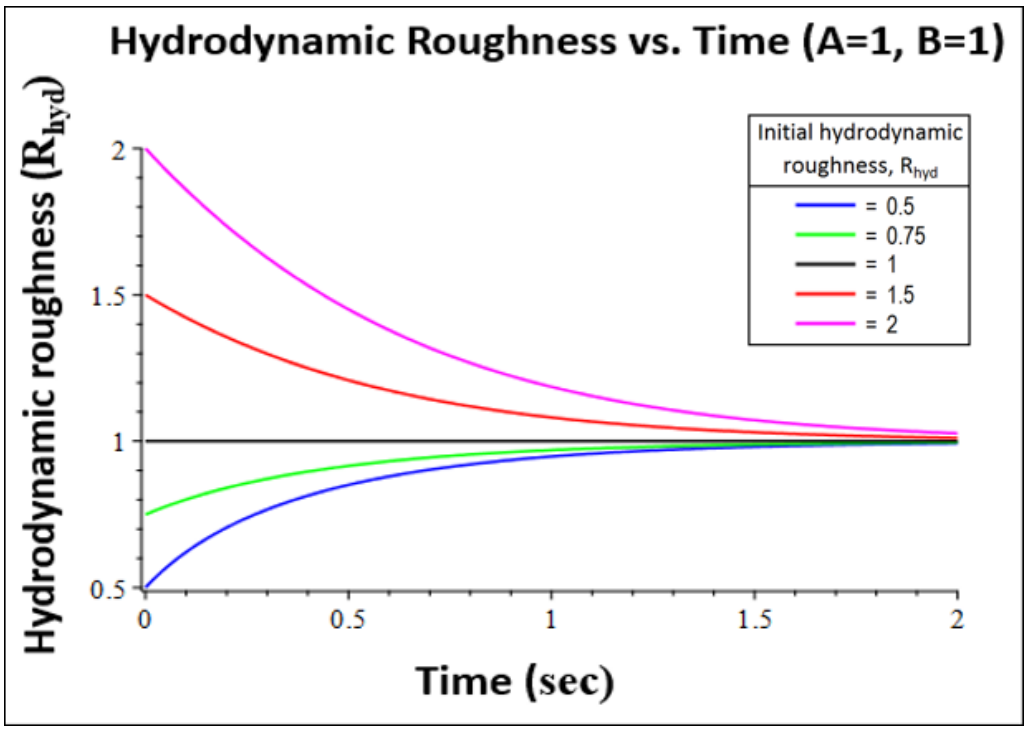

Figure 3.4, Hydrodynamic Roughness Vs. Time during the run-in Period

As can be seen in figure 3.4, hydrodynamic roughness always seeks an equilibrium value, while friction always decreases and also reaches its minimum value during run-in as shown in figure 3.3. Therefore, fluid self-organization during running-in results in a reduction in friction and wear to an equilibrium value.

3.4. Conclusion

It is shown in this chapter that in addition to the known phenomenon of surface self-organization in unlubricated friction, wetted frictional perimeters also undergo fluid self-organization and seek out optimal friction and wear values during run-in. With the formulations of equation 3.6, more optimal running-in schedules for tribological systems with fluid frictional interfaces can now be investigated by configuring mating parts with initial hydrodynamic roughness and fluid combinations which have self-organization characteristics. During the run-in time interval, these self-organizing tribological systems adjust until steady state equilibrium is reached.

4. Sliding Dry Friction Using a Pin-On-Disk Tribometer

4.1. Introduction

In this chapter a brief introduction to pin-on-disk tribometers and their use for measurement of tribological properties is presented followed by an in-depth analysis comparison between experimental friction results provided in a technical journal report and FEA calculations. Utilizing the same experimental parameters used in-situ for the authors friction measurement, FEA is performed and shown to follow a similar frictional trend during the first several seconds of run-in.

4.2. Pin-On-Disk Tribometers

The pin-on-disk tribometer is a commercially available test instrument used to evaluate tribological properties such as sliding wear and coefficient of friction of materials in relative rubbing movement against each other [1, 32]. The experimental arrangement is a three degree of freedom laboratory simulation which requires two test specimens, a pin and a disk positioned perpendicular to each other. Each degree of freedom is precisely controlled by programmable logic devices or computers which govern rotational motion for both test specimens and rate of dynamic pin loading through mechanical or fluid power action. Frictional force is usually measured with torque transducers or strain gages and amount of wear is determined by volume or weight loss after a certain sliding distance of the pin [33]. A groove is commonly machined into the disk to provide a sliding path for the pin to travel along, generate repeatability, and avoid alignment problems. The diameter and length of the pin or disk may be arbitrarily chosen, but size selection must ensure rigidity in order to avoid mechanical buckling or yielding [34]. Any combination of test specimen materials may be used and because of their relatively simple geometry, either the pin or disk can be easily manufactured.

The axial orientation of the pin-on-disk test setup can be either horizontal or vertical and for either arrangement, although not necessary, lubrication is introduced to the frictional interface to avoid undesirable dry running conditions. Consequently, for the horizontal rotating disk arrangement, the lubricant can be centrifugally flung out of the contact zone by windage and churning effects [33], and for the vertical rotating disk arrangement, the lubricant can fall out of the contact zone due to gravity [35]. Test specimen orientation can also affect the measurement of wear processes as a byproduct of wear debris discharge. In the horizontal arrangement, loose wear debris can fall into the pin wear track on the disk and be mechanically processed. The loose wear debris that is trapped in a frictional interface is known as the "third body mechanism" where the coefficient of friction may incorrectly increase because of plowing, or incorrectly decrease if the wear debris act as roller bearings [36]. Figure 4.1 shows a typical pin-on-disk test setup in the in the horizontally rotating disk arrangement.

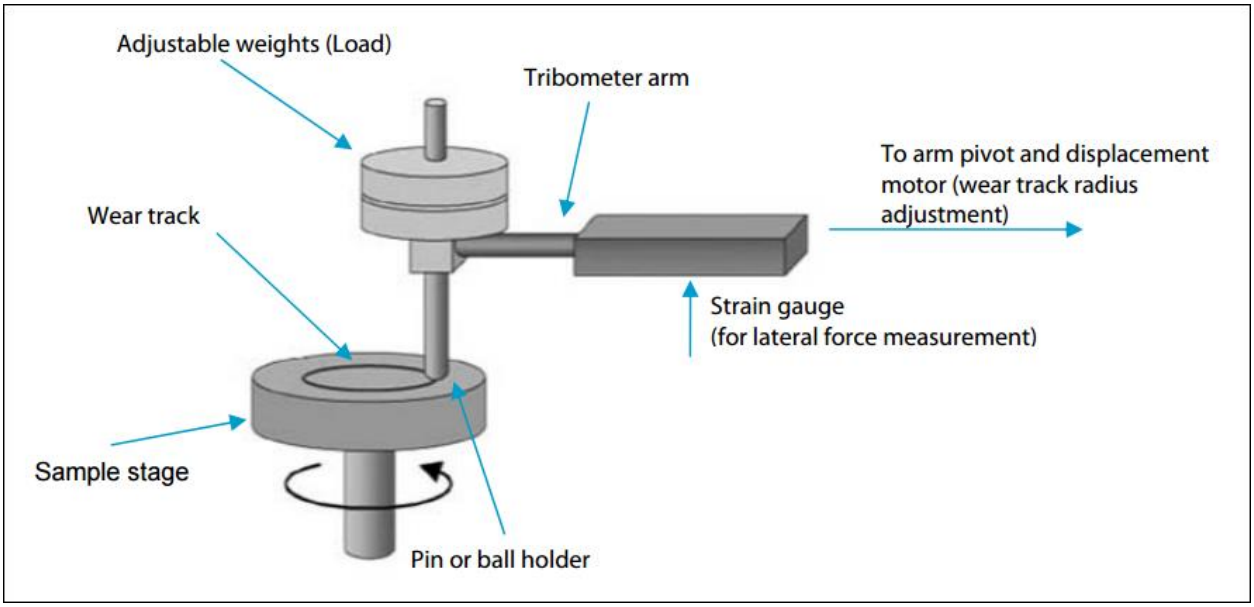

Figure 4.1, A Typical Pin-On-Disk Test Setup, [37]

Element Materials Technology (EMT), Nanovea, Anton-Paar, CSM as shown in figure 4.2 (recently acquired by Anton-Paar), Ducom, and CETR (recently acquired by Bruker), are among the numerous manufacturers of pin-on-disk tribometers that can readily accommodate a diverse range of controlled test parameters and atmospheres. This flexibility of distinct parameter accommodation used during testing, such as precise axial loading intensity, material selection, temperature, atmospheric pressure, sliding speed, and sliding distance is essential for accurate wear rate and coefficient of friction quantification [38]. Therefore, the use of commercial pin-on-disk tribometers can simulate to within a very close approximation, end use condition such as braking, and unlimited sliding in either direction.

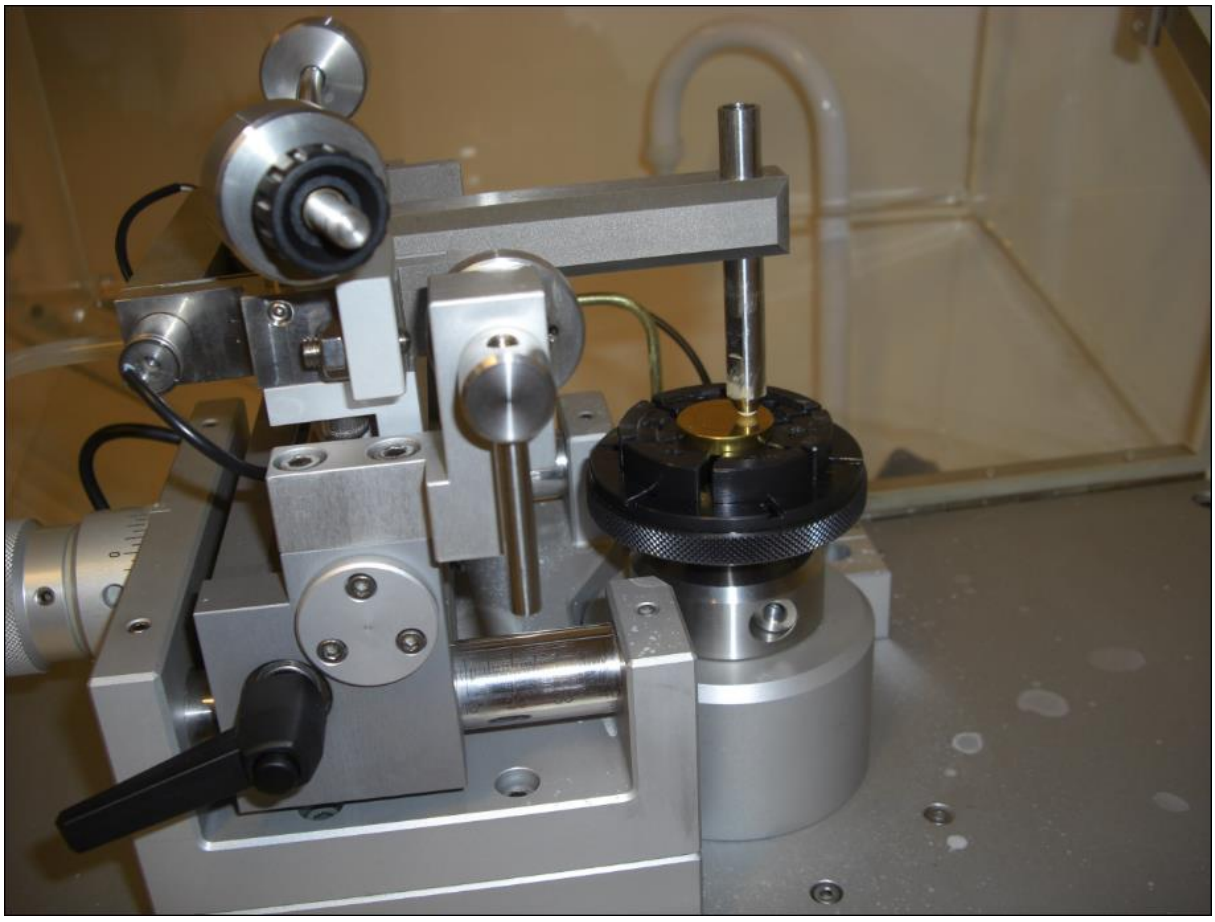

Figure 4.2, Pin-on-Disk Tribometer by CSM Instruments [39]

4.3. Mathematical Model

In order to investigate the transient friction response of dry sliding contact for a pin-on-disk tribometer, a comparison will be made between available pin-on-disk experimental data and finite element analysis using Solidworks Simulation. These experimental results were published in a technical paper by the Journal of Tribology which lists all of the parameters used for the measurement of the transient coefficient of friction for both green particulate fluids and unlubricated conditions [40]. These experimental parameters along with the mathematical model derived in this section will form the basis for initial conditions used in the FEA computational model.

By performing a torque balance using Newton's second law for rotational systems we can mathematically derive and predict the pin-on-disk's system behavior as it evolves over time. Assuming a horizontally oriented rigid disk undergoing sliding contact with an axially loaded pin that is parallel to and rotating about the disk's centerline, the derivation of the equation of motion for the system begins with the fundamental 2nd law equation:

$$\sum T = J \frac{d\omega}{dt} \tag{4.1}$$

In equation 4.1, $\sum T$ is the sum of the torques in the system measured relative to the centerline of the disk, ω is the angular velocity, and J is the moment of inertia of the pin. For the pin-on-disk dynamic frictional system there are two torques: one from the test apparatus supplied torque which provides pin rotation about the disk centerline and the other from the frictional torque at the pin and disk friction interface. Figure 4.3 illustrates the location of this frictional torque at the pin and disk contacting surfaces. The frictional torque is determined by multiplying the friction force μW by the pins radial distance to the centerline of the disk r. In

this experiment, the downward axial load, W is applied at a constant intensity and thus the equation for the frictional torque is provided by equation 4.2. Note that the frictional torque is given by $T_f = \mu W r$ only when the absolute value of the applied torque is equal or greater than the absolute value of $\mu W r$. Otherwise, the frictional torque is equal by absolute value to the applied torque, but has opposite sign. The naming convention used for the supplied torque to the rotating pin is provided in equation 4.3.

$$T_f = \mu W r \tag{4.2}$$

$$T = T_{app} \tag{4.3}$$

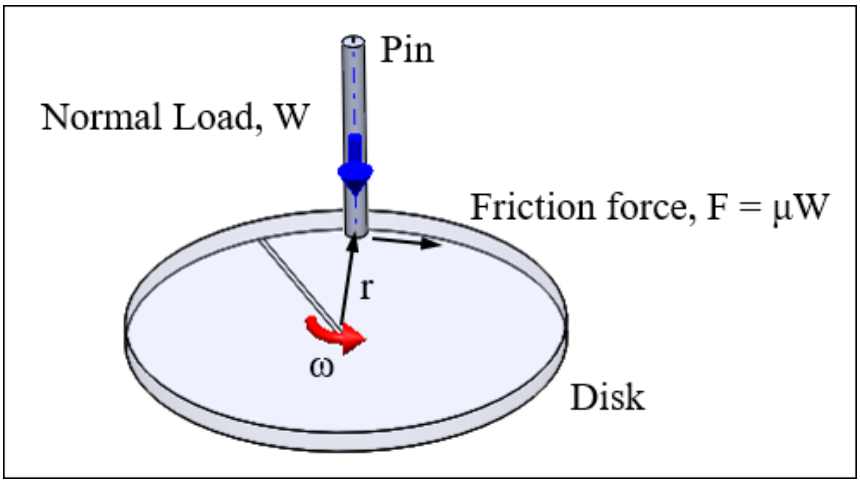

Figure 4.3, Pin on Disk Force Vector Diagram

By summing the two torques in equations 4.2 and 4.3, equation 4.1 becomes:

$$\sum T = T_{app} - \mu W r = J \frac{d\omega}{dt} \tag{4.4}$$

where, μ is the coefficient of friction and ω is the pin's angular velocity with units $\frac{rad}{sec}$.

For a pin rotating a radial distance from an axis the moment of inertia for point mass contact is given by $J = mr^2$ where *r* is the pin's radial distance to the disks centerline and m is the pin's mass.

Assuming that the coefficient of friction is a function of velocity we may use the relation:

$$\mu = \mu_0 - \alpha|V| \tag{4.5}$$

where, μ_0 is the static coefficient of friction and α is a friction parameter. Furthermore, assuming that velocity is positive, or $V > 0$ and noting that $V = \omega r$, Eq. 4.5 becomes:

$$\begin{aligned} \mu &= \mu_0 - \alpha V \\ \mu &= \mu_0 - \alpha(\omega r) \end{aligned} \tag{4.6}$$

With this new definition for the coefficient of friction, equation 4.4 becomes:

$$\begin{aligned} T_{app} - (\mu_0 - \alpha\omega r)Wr &= J\frac{d\omega}{dt} \\ T_{app} - \mu_0 Wr + \alpha\omega Wr^2 &= J\frac{d\omega}{dt} \end{aligned} \tag{4.7}$$

Equation 4.7 is a first-order linear ordinary differential equation with constant coefficients. Its complete solution is represented by the sum of two parts; the homogeneous part which describes the transient response of the system and the particular part which describes the steady state. Therefore, the solution to equation 4.7 will be of the form; $\omega(t) = \omega_t + \omega_{ss}$.

Because the homogeneous part of the solution contains only the terms that depend on time, the equation to be solved for the transient state is:

$$J\frac{d\omega}{dt} - \alpha\omega Wr^2 = 0 \tag{4.8}$$

which is solved by using separation of variables:

$$\frac{d\omega}{\omega} = \frac{\alpha W r^2}{J} dt \Rightarrow$$
$$\int \frac{1}{\omega} d\omega = \frac{\alpha W r^2}{J} \int dt \Rightarrow$$
$$\ln(\omega) = \frac{\alpha W r^2}{J} t + C$$

Because we are solving for ω, we can rewrite the above equation in exponential form as:

$$\omega(t) = e^{\frac{\alpha W r^2}{J} t + C} = e^C e^{\frac{\alpha W r^2}{J} t}$$

To solve for the constant of integration, we may apply the initial condition of the angular velocity by assuming that at time $t = 0$, the angular velocity is a constant value, or $\omega = \omega_0$. Therefore:

$$\omega(t = 0) = \omega_0 = e^C e^{\frac{\alpha W r^2}{J} t} = e^C e^0 = e^C \Rightarrow$$
$$\omega_0 = e^C \Rightarrow$$
$$\omega_t = \omega_0 e^{\frac{\alpha W r^2}{J} t}$$

The next step to determining the general solution to equation 4.7 is to find the particular term which describes the steady state processes of the system which is unchanging in time. The equation to be solved for the particular part of the system is:

$$T_{app} - \mu_0 W r = -\alpha \omega W r^2 \tag{4.9}$$

which has the steady state solution:

$$\omega_{ss} = \frac{\mu_0}{\alpha r} - \frac{T_{app}}{\alpha W r^2}$$

Therefore, the solution to the pin-on-disk system equation is:

$$\omega(t) = \omega_0 e^{\frac{\alpha W r^2}{J} t} + \frac{\mu_0}{\alpha r} - \frac{T_{app}}{\alpha W r^2}$$
$$\omega(t) = \omega_0 e^{\frac{\alpha W}{m} t} + \frac{\mu_0}{\alpha r} - \frac{T_{app}}{\alpha W r^2} \quad (4.10)$$

Equation 4.10 describes the angular velocity of the pin with time. In the technical paper on pin-on-disk transient friction characteristics of green particulate fluids, a constant sliding speed of 100 mm/sec is provided, therefore we must modify equation 4.10 to conform to a linear velocity definition. Since $V = \omega r$, or in other words: $\omega = \frac{V}{r}$, equation 4.10 becomes:

$$\frac{V_1}{r} = \frac{V_0}{r} e^{\frac{\alpha W}{m} t} + \frac{\mu_0}{\alpha r} - \frac{T_{app}}{\alpha W r^2}$$
$$V_1 = V_0 e^{\frac{\alpha W}{m} t} + \frac{\mu_0}{\alpha} - \frac{T_{app}}{\alpha W r} \quad (4.11)$$

In Equation 4.11, V_1 is the final velocity, or 100 mm/sec as stated in the experimental initial conditions. By solving this equation for T_{app}, a value for the torque required to rotate the pin from rest to 100 mm/sec in 2 seconds can be determined. This calculated torque is then used in the FEA analysis for the transient friction response in the next section.

4.4. Computational Model

The pin and the disk 3D CAD models of the pin-on-disk tribometer test setup are modeled in Solidworks and then mated together into an assembly model used for the transient friction FEA computations. Model creation begins with a dimensioned planar sketch and then an axial solid revolve is performed which provides model volume. Material properties are then given to each part in order to provide component stiffness for the FEA computation. Following

the experimental setup, the pin is defined as copper and the disk is defined as aluminum. Figures 4.4 and 4.5 show the pin and disk models that are used in the FEA.

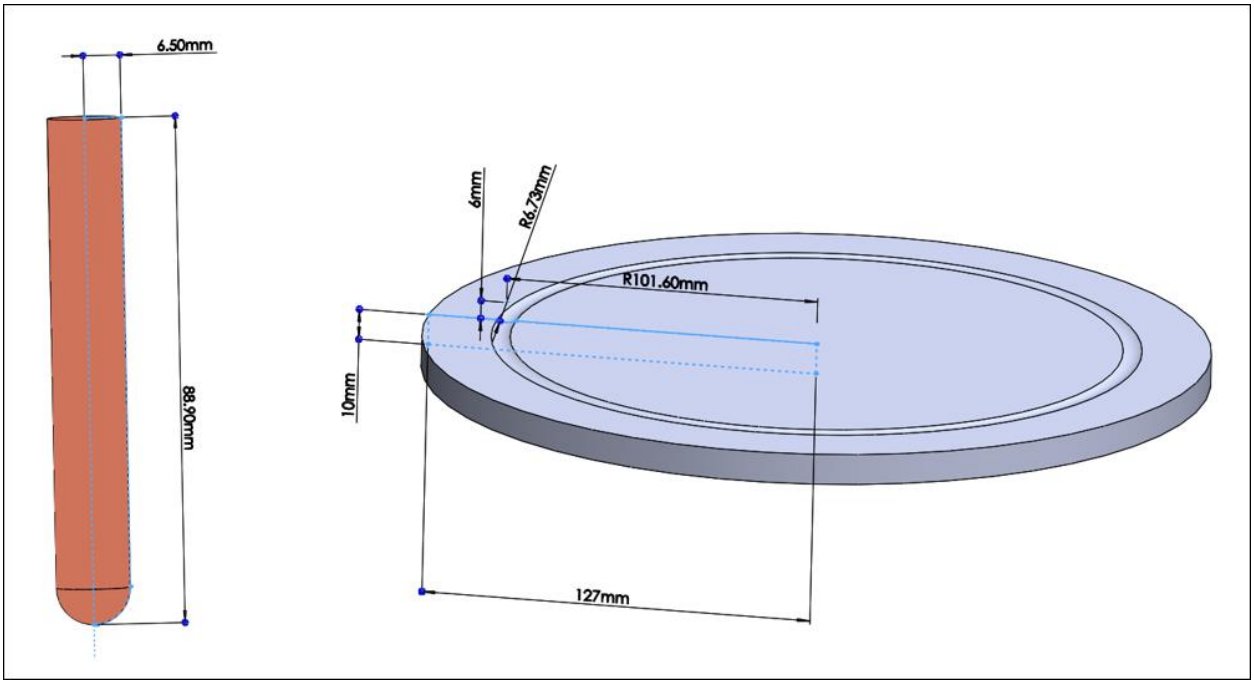

Figure 4.4, Pin and Disk 3D CAD Models

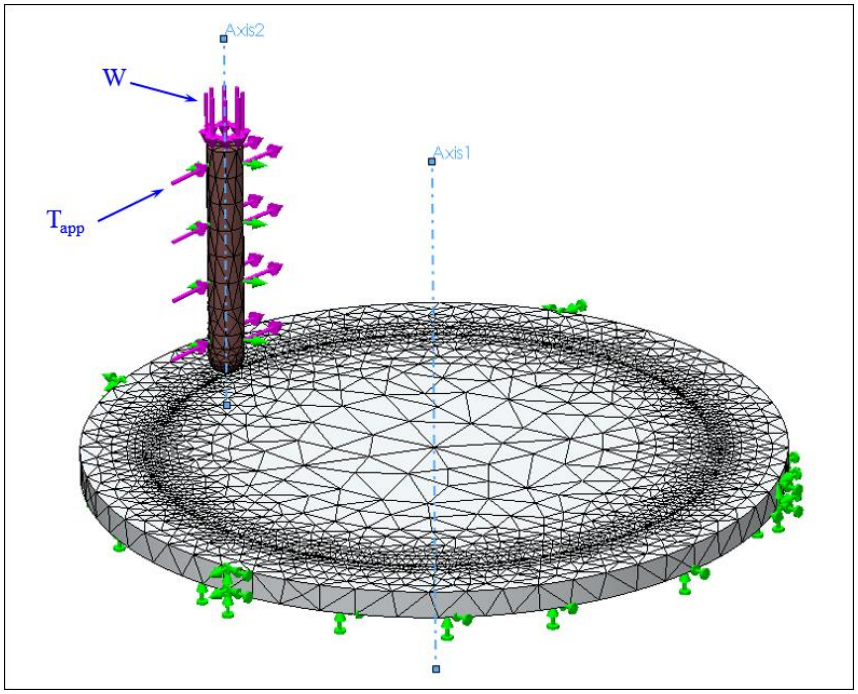

Figure 4.5, Pin-on-Disk FEA Computational Model with Initial Conditions Shown

Figure 4.5 shows the FEA computational model used for the transient friction calculations where the green arrows represent constrained areas of the model and the purple arrows represent areas of loading. The bottom and side of the disk is constrained from any movement, in close approximation to being rigidly pressed and mounted into a table or fixture. The cylindrical face of the pin is radially constrained preventing any radial growth of the pin, in close approximation of being held by a clamping fixture. A vertically downward constant axial load is applied to the top of the pin and torque is applied to the cylindrical face of the pin about the disk centerline.

Linear elastic material properties are used with a modulus of elasticity of 69 GPa, yield strength of 0.055 GPa, and Poisson's ratio of 0.33 defined for the aluminum disk and a modulus of elasticity of 110 GPa, yield strength of 0.259 GPa, and Poisson's ratio of 0.37 defined for the copper pin. There are 7,443 TETRA10 elements in the FEA model with a maximum mesh size of 20 mm, minimum mesh size of 10 mm, and a 3 mm mesh refinement specified at the disk wear track and the radiused tip of the pin. No penetration contact is defined between the wear track of the disk and radiused tip of the pin with a value given for the static coefficient of friction, μ_0. Table 4.1 lists the parameters used for three separate FEA calculations with the static coefficient of friction being the only value changed for each calculation. Defining μ_0 = 0.95, 0.55, & 0.15 for the three load cases, all other values remain the same and the transient friction response for each load case is plotted in figure 4.7. Motivation for selecting these static coefficient values will be discussed in the conclusion found in section 7.1.

Table 4.1, Pin-On Disk Simulation Parameters

Pin-on-disk simulation parameters		
Parameter	**Value**	**Units**
Pin diameter, D_p	13	mm
Pin Length, L_p	89	mm
Pin mass, m_p	100	g
Disk diameter, D_d	254	mm
Disk Length, L_d	10	mm
Initial velocity, V_0	0	mm/s
Final velocity, V_1	100	mm/s
Pin axial load, W	0.981	N
Pin radial distance, r	102	mm
Friction parameter, α	6.80E-04	s/mm
Applied torque, T_{app}	40,000	N-mm

In order to determine the value for torque to apply to the cylindrical face of the pin about the disks axis, T_{app} is solved for in equation 4.11. Then using the parameters listed in table 4.1, the value for T_{app} is calculated.

$$T_{app} = \alpha W r \left(V_0 e^{\frac{\alpha W}{m} t} + \frac{\mu_0}{\alpha} - V_1 \right) \Rightarrow$$

$$T_{app} = (0.68)(0.981)(0.102)\left[(0.001) e^{\frac{(0.68)(0.981)}{(0.1)}(2)} + \frac{(0.95)}{(0.981)} - 0.1 \right] \Rightarrow$$

$$T_{app} = 40 Nm$$

To simulate system run-in, a linear torque time curve is applied with zero torque at equipment start up and final torque reached at 2 seconds. It is assumed that once the pin velocity of 100 mm/sec has been reached, the torque is held constant at this value for the duration of equipment operation. Figure 4.6 shows the torque time curve used in the FEA computations.

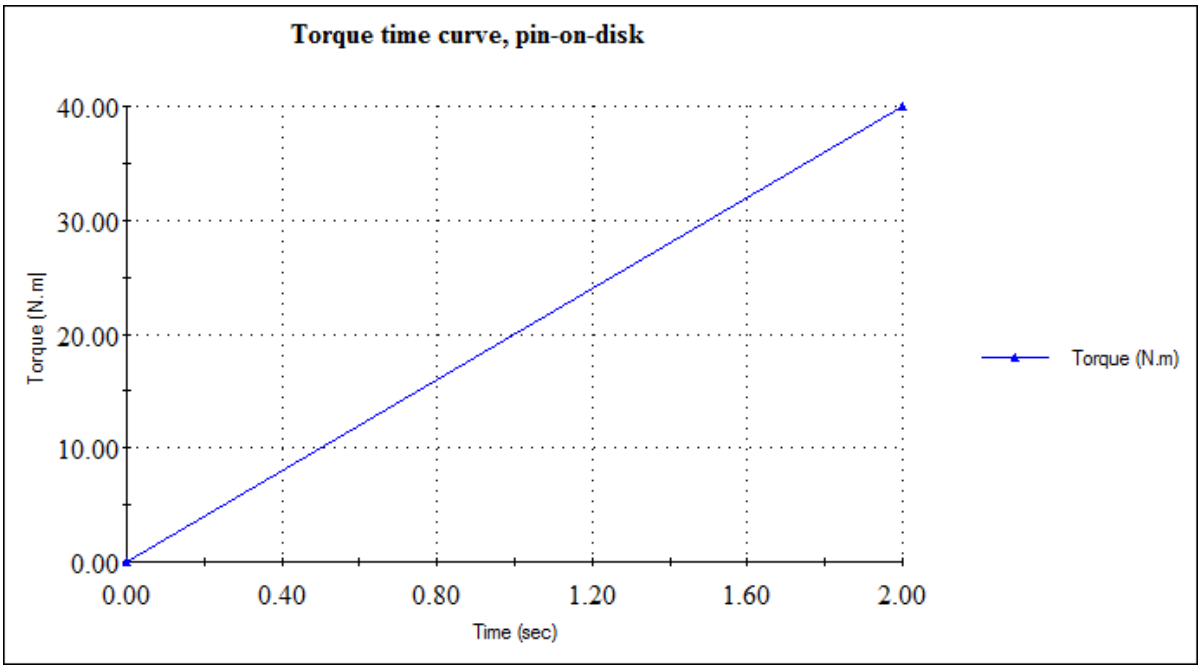

Figure 4.6, Load Time Curve for the Pin-on-Disk FEA

4.5. Results

Using the initial parameters listed in table 4.1, the transient friction force for the pin-on-disk test setup is shown in figure 4.7. The contact friction force is measured at the frictional contact interface of the disk wear track and radiused tip of the pin and plotted for the length of time of the solution run. Because of the coefficient of frictions linear relationship with the normal applied load, dividing this friction force by the constant downward vertical load on the pin at each time step yields a transient coefficient of friction. Figures 4.8 and 4.9 show the von Mises stress distribution and contact pressure plots at the final time step (t = 2 sec).

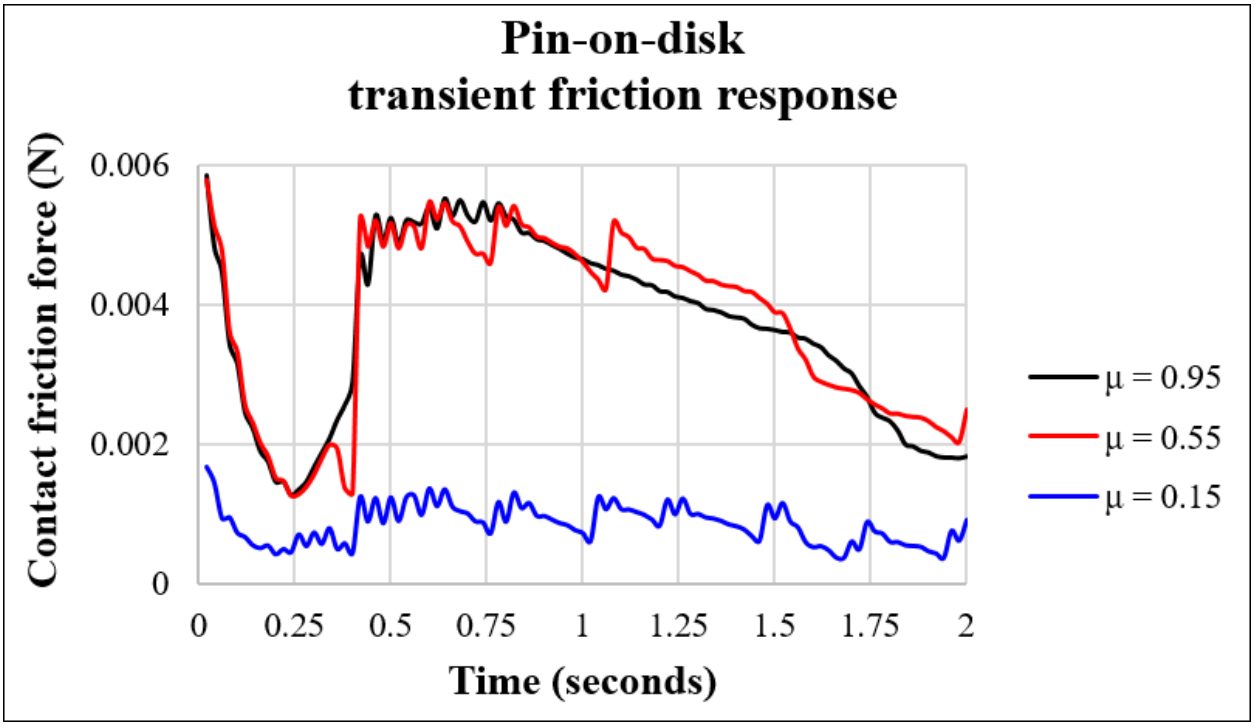

Figure 4.7, Resultant Contact Force at the Pin and Disk Contacting Surface

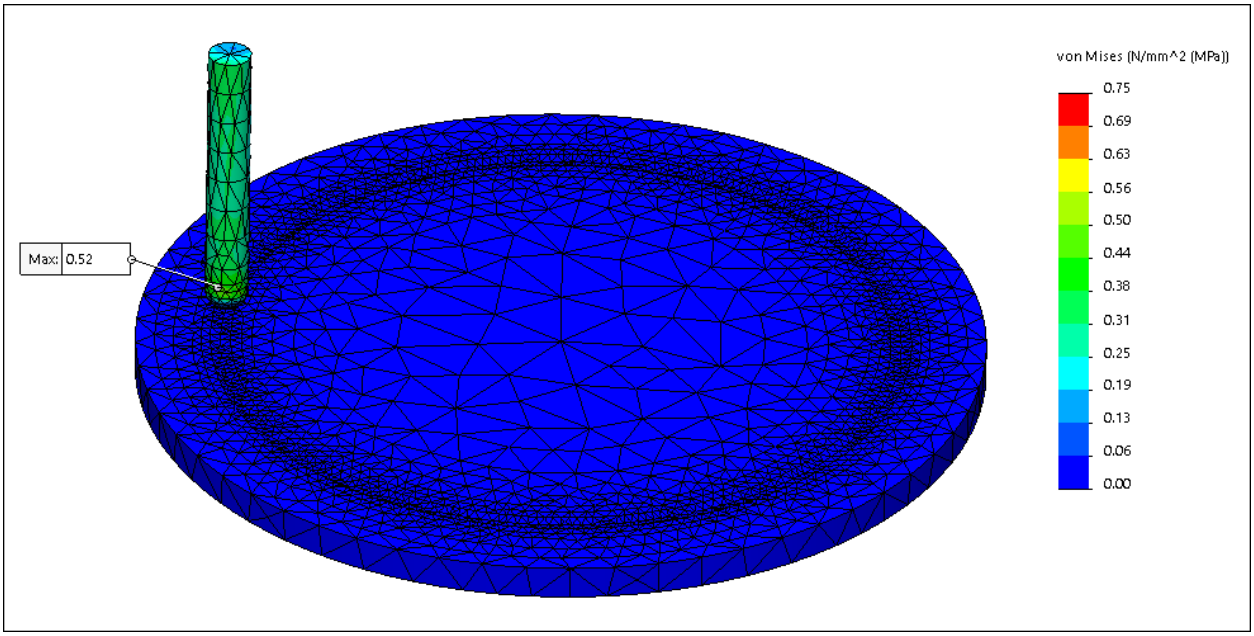

Figure 4.8, von Mises Stress Distribution at Final Time Step, Pin-On-Disk, μ=0.95

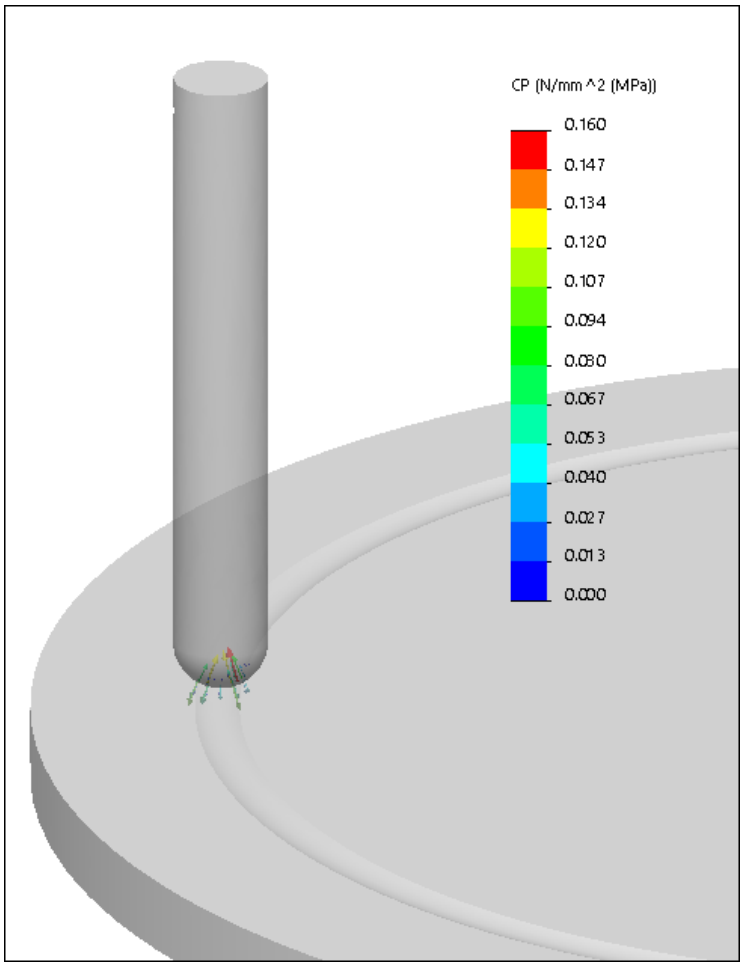

Figure 4.9, Contact Pressure Plot at Final Time Step, Pin-On-Disk, μ=0.95

Because the von Mises stress distribution has a maximum value that is below material yield limit with margin, the justification for using linear material properties in the FEA is validated.

4.6. Conclusion

In figure 4.7 a transient friction response curve for the pin-on-disk frictional interface is shown for a total running time of 2 seconds using three different static coefficient of friction values. Comparing these plots with the experimental coefficient of friction plot from the technical report shown in figure 4.10 for unlubricated conditions, we see a common trend between both curves where initially, the friction is at a maximum value and then decreases as the physics in the system progresses in time. This downward frictional tendency suggests that there is some degree of mechanical run-in before steady state is reached even for dry sliding conditions.

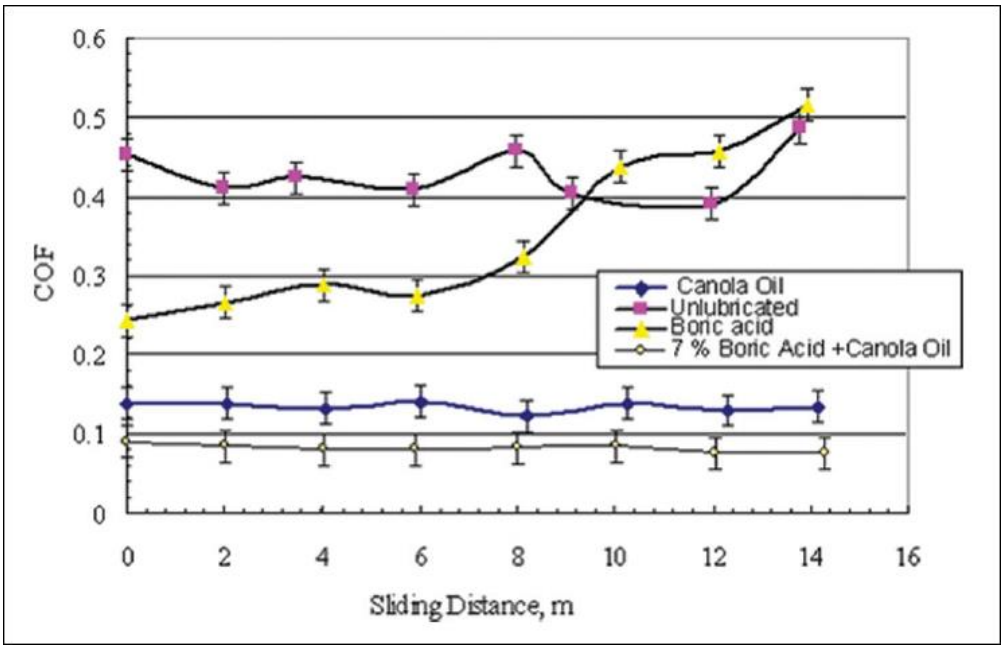

Figure 4.10, Experimental Coefficient of Friction Results [40]

5. Rotating Contact Friction in a Rotating Shaft and Journal Bearing Assembly

5.1. Introduction

In this chapter, the transient frictional response for dry rotating contact between a plain journal bearing and shaft assembly is computed using FEA. Following a brief introduction to common industrial applications for journal bearing and shaft arrangements, an in-depth analysis comparison between available experimental friction results from a technical journal for dry sliding journal bearing contact and FEA computations is made. Utilizing the same experimental parameters used in-situ for the authors friction measurement, FEA is performed and shown to follow a similar frictional trend during the first several seconds of run-in

5.2. Industrial Applications of Plain Journal Bearings

Journal bearings, otherwise known as bushings facilitate rotation, translation, or a combination of both motions by means of a shaft, otherwise known as a journal which are assembled cylindrically concentric with one another. The relative motion between the shaft and bearing is sliding contact with no axial (thrust) loading resistance. Because shaft diameter is usually fixed by strength and deflection requirements, it is the bearings length that is designed to satisfy a parameter called the length to diameter ratio, or l / d ratio. Suggested l / d values for journal bearings are usually between 1 and 2 [41], however values as low as 0.25 are also considered satisfactory under average operating conditions [4]. Table 5.1 lists suggested journal bearing l / d ratios used in various applications. Diametral clearance between the journal bearing and shaft is also another important design parameter to consider when sizing bearing dimensions for a tribological system. A sufficient gap between the bearing and the shaft is required in order

to allow for thermal expansion of the lubricant and components as they tend to heat up over time. A complete lubrication analysis is suggested for determining the optimum diametral clearance and thus, manufacturing dimensions. Figure 5.1 shows a common journal bearing and shaft arrangement supported by roller bearing pillow blocks at each shaft end. Radial movement of the shaft is constrained by the bearing bore and set screws within the pillow block bearings tighten against the shaft, so that only shaft rotation is allowed. A plate or other mechanical attachment is usually mounted onto the bushing for axial or circumferential positioning or guiding. If a pair of journal bearing and shaft arrangements are used in parallel, only axial positioning is permitted.

Table 5.1, Suggested L / D Values for Journal Bearings [41]

Suggested L / D Ratios For Journal Bearings Used In Various Applications			
Type of Service	*l / d*	Type of Service	*l / d*
Gasoline and diesel engine		Light shafting	2.5 to 3.5
Main bearings and crankpins	0.3 to 1.0	Heavy shafting	2.0 to 3.0
Generators and motors	1.2 to 2.5	Steam engine	
Turbogenerators	0.8 to 1.5	Main bearings	1.5 to 2.5
Machine tools	2.0 to 3.0	Crank and wrist pins	1.0 to 1.3

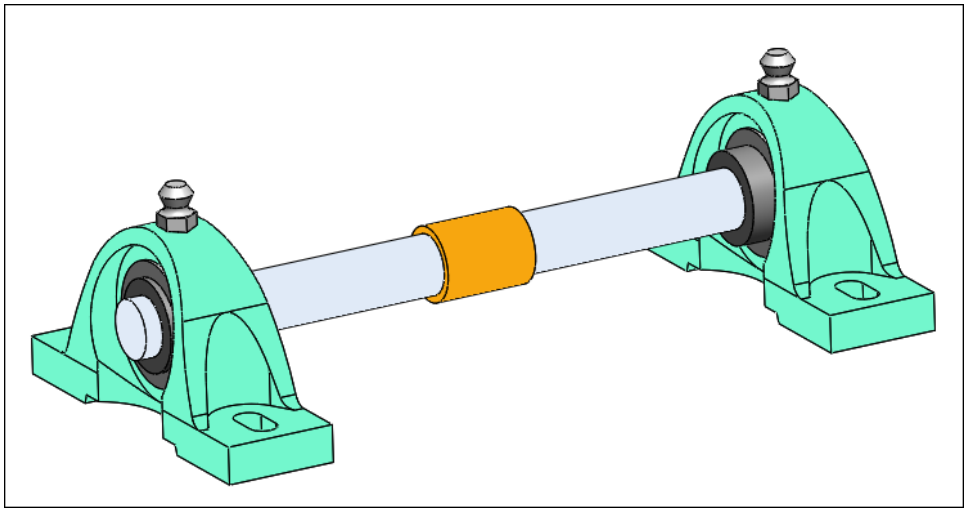

Figure 5.1, Common Shaft and Journal Bearing Assembly

Because of their abundant versatility, journal bearings are used in various types of machinery and equipment that have a wide range of design requirements [42]. Some of the factors which influence their use include lubrication availability, load intensity, speed, and misalignment allowance. In a majority of industrial applications, the sliding surfaces of journal bearings either require forced lubrication or are made of a self-lubricating bearing alloy material such as Oilite, a sintered porous bronze alloy internally impregnated with oil lubricant which was developed by Chrysler Corporation in 1930 [43]. There are however, unique applications where lubrication is not allowed and thus dry sliding journal bearings are required such as in aerospace where temperatures exceed the flashpoint for certain lubricants and in the food and pharmaceutical industries where contamination from lubricants create unsanitary conditions [44]. However with recent advancements of SAE 841 and SAE 863, oil embedded food grade bushings that meet USDA regulations are now commercially available [45, 46].

Common materials used for dry sliding bearing materials include steel, aluminum, brass, nylon, ultra-high molecular weight polyethylene (UHMW) and, polytetrafluoroethylene (PTFE) which is commonly referred to as Teflon. Manufacturers of thermoplastic journal bearings usually recommend including a run-in process so that some of the softer bearing material can coat itself onto the shaft [47, 48]. The wear debris that result from the shearing of bearing surface asperities during run-in and throughout the duty cycle serves as a lubricating layer between the bearing and the shaft increasing the systems lubricity [49].

5.3. Mathematical Model

In order to investigate the transient friction response of a stationary journal bearing and rotating shaft assembly, a comparison will be made between the FEA calculations performed in this chapter and available experimental data of the dry sliding coefficient of friction for a mild steel journal bearing and shaft arrangement. These experimental results were published in a technical paper published by the Institute for Natural Sciences and Engineering [50] which lists all of the experimental parameters used for the measurement of the transient coefficient of friction of fixed journal bearing and rotating shaft arrangements. These experimental parameters will form the basis for the initial conditions used in the FEA computational model.

The equation of motion for a fixed shaft and rotating bearing arrangement are similar to the equations of motion derived for the pin-on-disk test setup in section 4.3. In that section, the mathematical derivation for the equations of motion was required in order to calculate the proper torque to apply in the FEA computational model. For the FEA computations performed in this chapter, the initial conditions are readily available in the description of the experimental setup used in the technical report which provide the loading and constraints needed for the mathematical model.

5.4. Computational Model

The journal bearing and shaft arrangement for the FEA computations are modeled in Solidworks using the same solid revolve method about the components axis that was used in section 4.4. Figure 5.2 shows the journal bearing and shaft models that are used in the FEA, where it can be seen that split lines are modeled onto both models for loading and constraining the parts in the FEA. The split lines on each end of the shaft represent bearing seats, and the split

lines on the journal bearing symmetrically divide the top and bottom of the bearing for longitudinal loading.

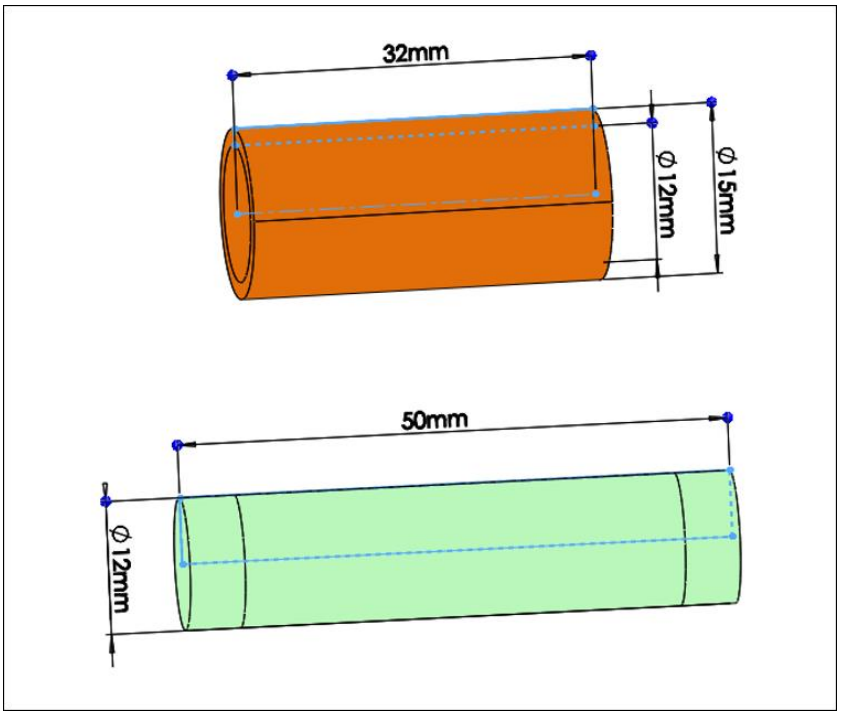

Figure 5.2, Journal Bearing and Shaft 3D CAD Models

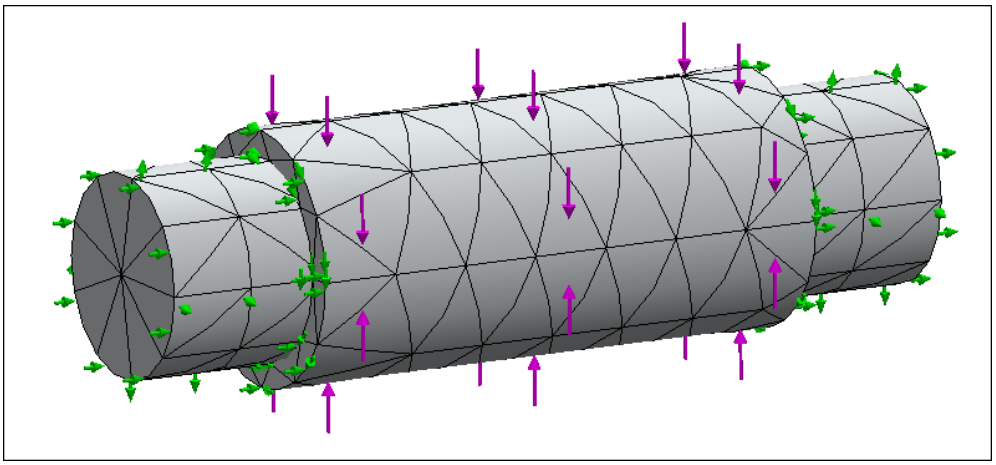

Figure 5.3, Journal Bearing and Shaft FEA Model with Initial Conditions Shown

Figure 5.3 shows the FEA computational model used for the transient friction calculations of the journal bearing and rotating shaft arrangement where the green arrows represent constrained areas of the model and the purple arrows represent areas of loading. The journal bearing is axially and rotationally constrained on both ends, so that only radial movement is allowed. Both bearing seats on the shaft are radially constrained and both ends of the shaft are axially constrained allowing only rotational motion. A rotational displacement is applied to the shaft outside diameter which will allow the shaft to rotate 1 radian, or approximately 60 degrees in 2 seconds. A 1 kg vertical load is applied equally and in opposite directions to each bearing half.

Linear elastic material properties are used with a modulus of elasticity of 200 GPa, yield strength of 0.352 GPa, and Poisson's ratio of 0.29 defined for the AISI 1020 steel bearing and shaft. There are 3,898 TETRA10 elements in the FEA model with a mesh size of 5 mm. No penetration contact is defined between the bearing and shaft interfacing diameters with a value given for the static coefficient of friction, μ_0. Table 5.2 lists the parameters used for three separate FEA calculations with the static coefficient of friction being the only value changed for each load case. Defining μ_0 = 0.95, 0.55, & 0.15 for the three load cases, all other values remain the same and the transient friction response for each load case is plotted in figure 5.5.

Table 5.2, Journal Bearing and Shaft Simulation Parameters

Journal bearing and shaft simulation parameters		
Parameter	**Value**	**Units**
Shaft diameter, D_s	12	mm
Shaft length, L_s	50	mm
Bearing outside diameter, D_{bo}	15	mm
Bearing inside diameter, D_{bi}	12	mm
Bearing length, L_b	32	mm
Bearing vertical load, W	1	kg
Initial shaft rotational displacement, θ_1	0	rad
Final shaft torque, θ_2	1	rad

To simulate system run-in, a linear rotation time curve is applied to the shaft with zero displacement at equipment start up and final displacement reached at 2 seconds. Figure 5.4 shows the rotation time curve used in the FEA computations.

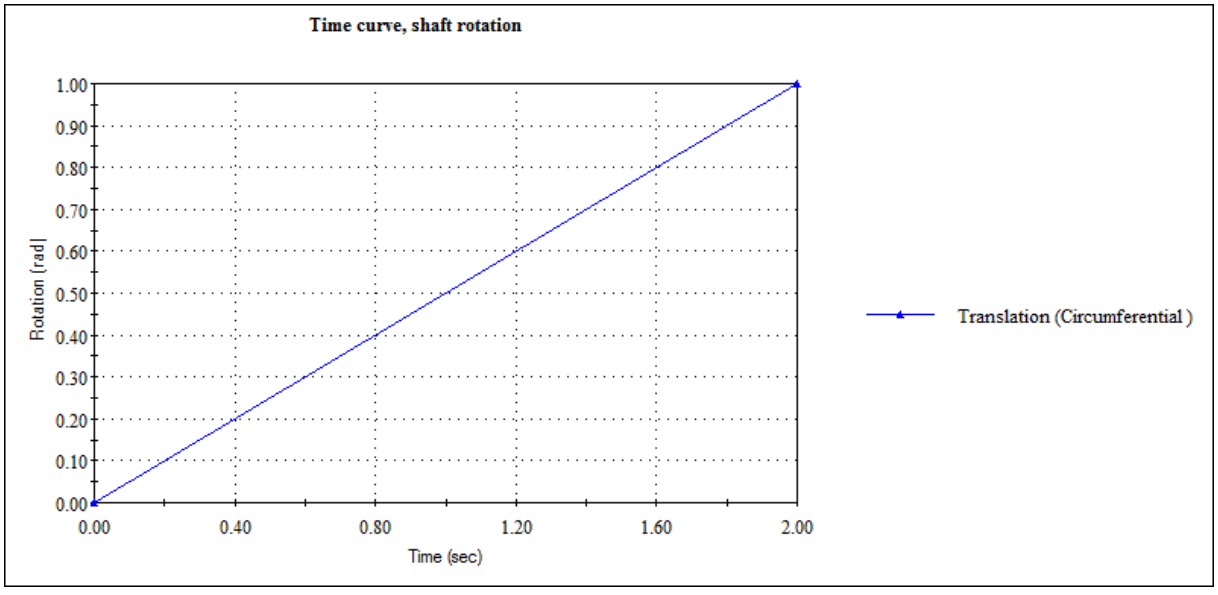

Figure 5.4, Load Time Curve for the shaft / journal bearing FEA

5.5. Results

Using the initial condition parameters listed in table 5.2, the transient friction force at the journal bearing and shaft contacting surface is shown in figure 5.5. The contact friction force is measured at the contact interface between the outside diameter of the shaft and the inside diameter of the journal bearing for the length of time of the solution run. Figures 5.6 and 5.7 show the von Mises stress distribution and contact pressure plots at the final time step (t = 2 sec).

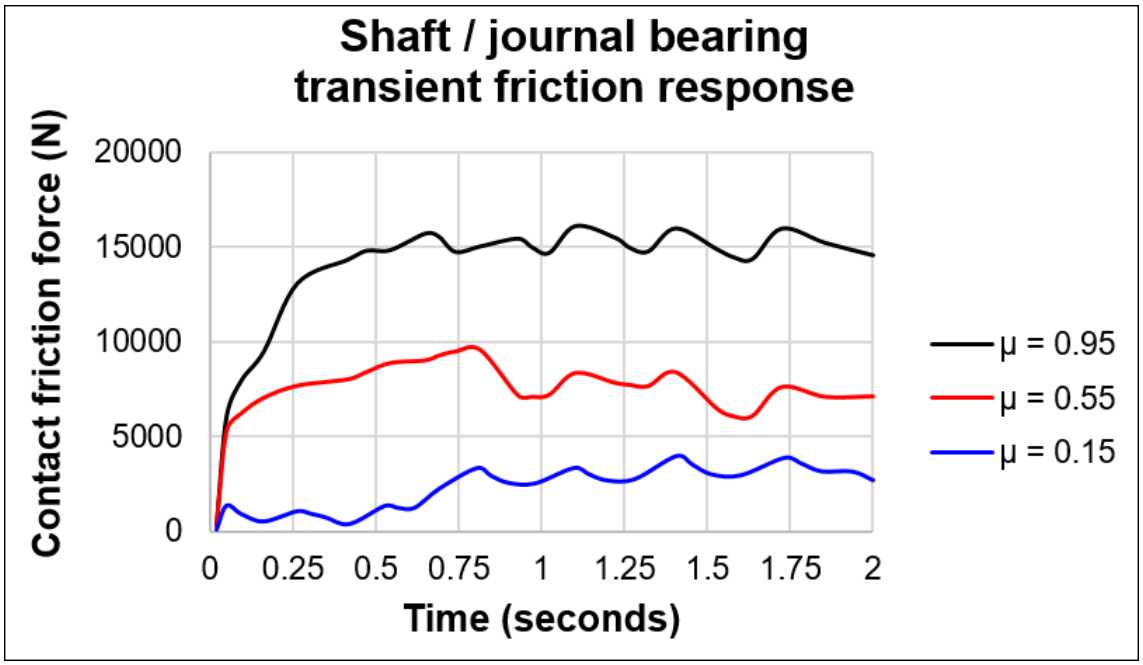

Figure 5.5, Resultant Contact Force at the Journal Bearing and Shaft Contacting Surface

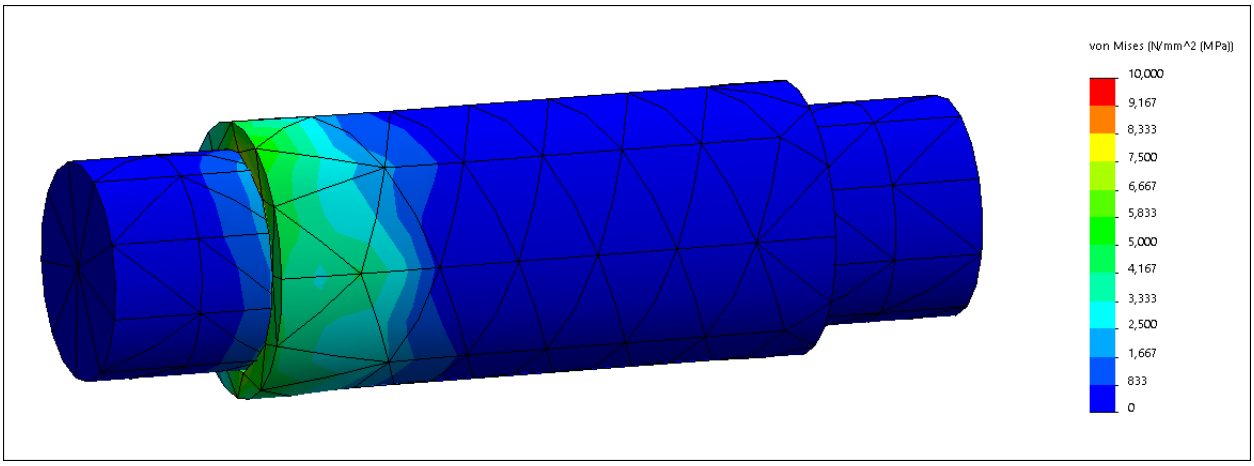

Figure 5.6, von Mises Stress Distribution at Final Time Step, JRNL BRG and Shaft, μ=0.95

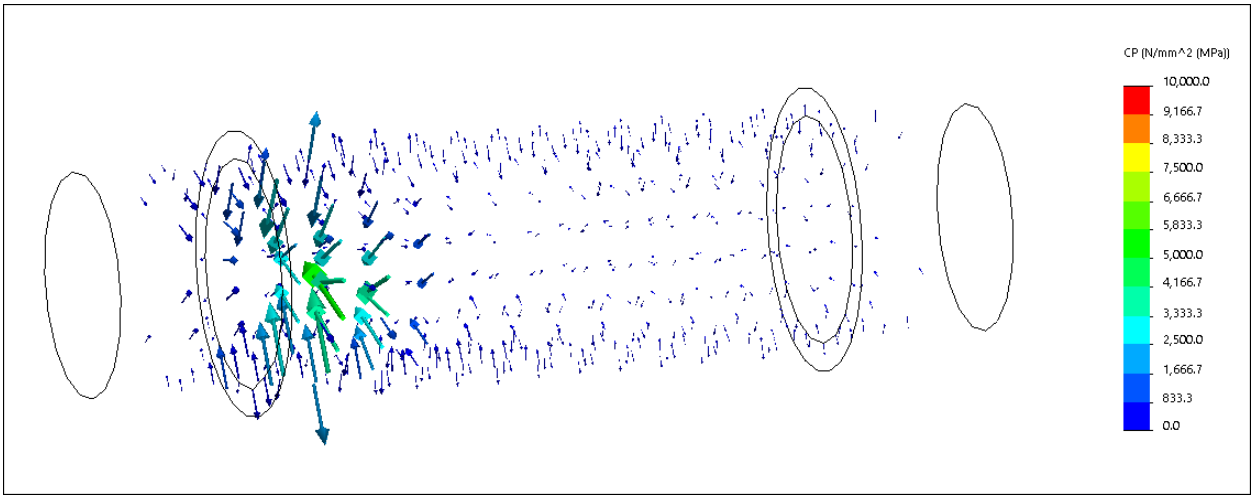

Figure 5.7, Contact Pressure Plot at Final Time Step, Journal BRG and Shaft, μ=0.95

Because the von Mises stress distribution has a maximum value that is below material yield limits with margin, the justification for using linear material properties in the FEA is validated.

5.6. Conclusion

In figure 5.5 a transient friction response curve for the journal bearing and shaft frictional interface is shown for a total running time of 2 seconds with three different static coefficient of friction values used. Comparing this plot with the experimental coefficient of friction with increasing shaft speed plot shown in figure 5.8, we see a common trend among both curves where the friction increases with increasing speed as the physics in the system progresses in time. As in the case for the pin-on-disk transient friction presented in chapter 4, the changing frictional tendency at start up suggests that there is some degree of mechanical run in before steady state is reached for journal bearings undergoing dry rotating friction.

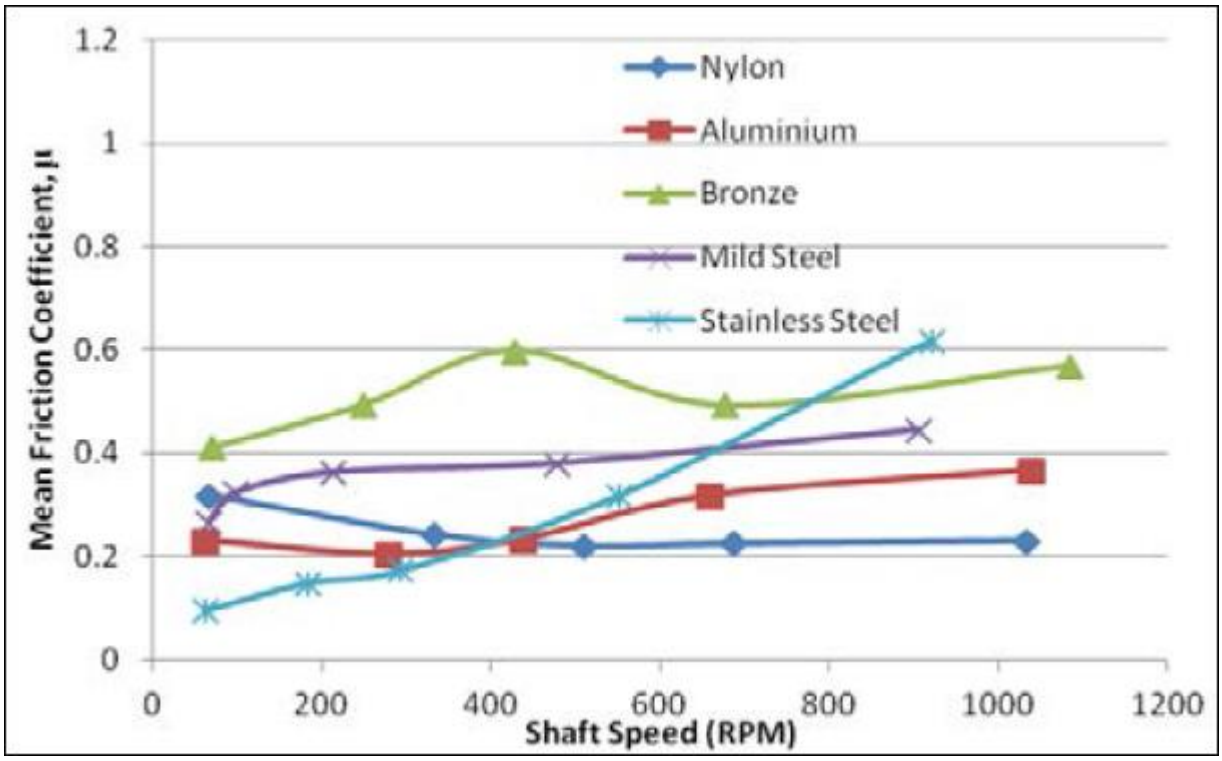

Figure 5.8, Experimental Coefficient of Friction Results [50]

6. Sliding Contact Friction in a Piston - Cylinder Arrangement

6.1. Introduction

In this chapter we investigate the transient frictional response for dry sliding contact at the frictional interface between a piston ring pack and cylinder bore. Following a brief introduction to piston-cylinder arrangements and their common use in industrial applications, an in-depth analysis is performed by modeling the components using CAD software with design recommendations provided in the *Tribology Handbook* by Neale [51]. Using these computer models, FEA computations are then performed and a transient frictional plot is calculated.

6.2. Industrial Applications of Piston - Cylinders

Cylinders used in mechanical systems serve as the space that pistons linearly oscillate in. Piston rings are securely pressed onto machined grooves on the piston outer diameter and seat against the inside of the cylinder bore to ensure axial alignment during travel. The piston-cylinder arrangement can be found in many different types of industrial applications such as in hydraulic or pneumatic power where a column of fluid pressure fills the closed end of a cylinder and presses against the piston causing linear actuation. In this case, the piston either provides a pressing force commonly required in hydraulic presses, or positional placement through stroke. The piston-cylinder arrangement is also used in the internal combustion engine where a reciprocating piston travels inside of a cylinder which acts as a combustion chamber with a mixture of air and fuel as the working fluid as shown in figure 6.1. Actuation of the piston is caused by an explosion from the air-fuel mixture driving the piston to the left towards bottom dead center. A flywheel rotational energy storage device propels the piston to the right towards top dead center, completing the cycle.

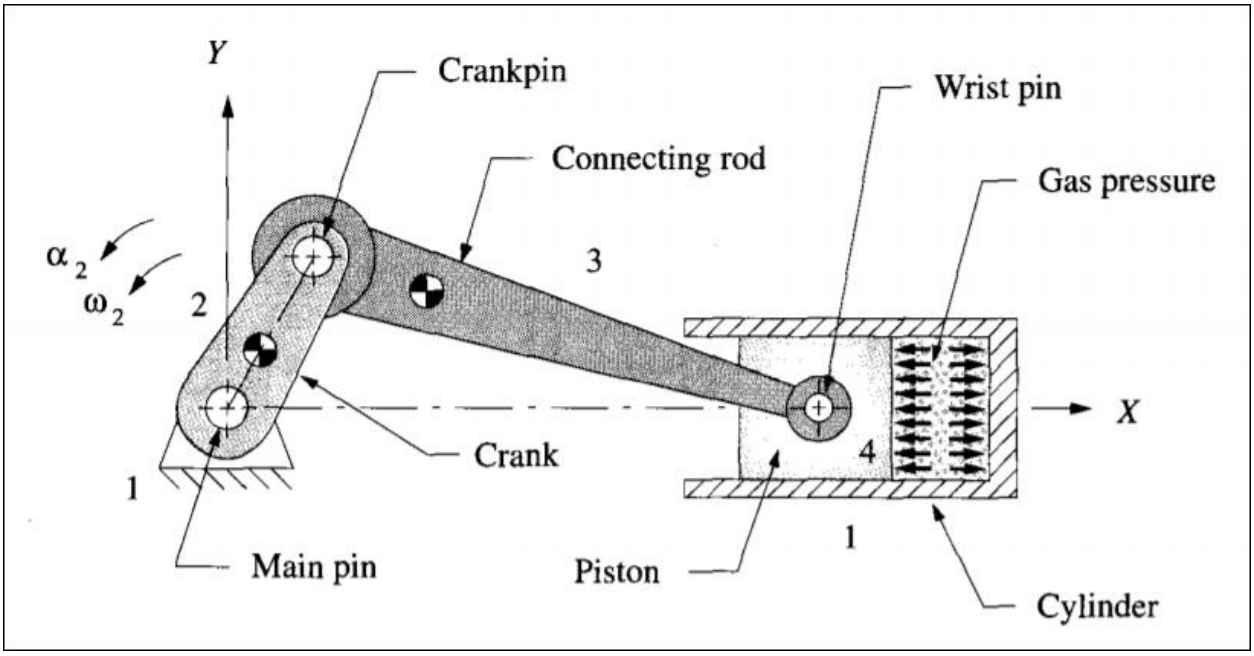

Figure 6.1, Piston-Cylinder Arrangement in Action in an Internal Combustion Engine [52]

Because these devices can see millions of cycles in their lifetime, friction and wear are important properties to understand during the run-in period and thus serves as the basis for the motivation of its analysis in the following section.

6.3. Mathematical Model

The transient frictional response for a typical piston / cylinder arrangement found in an internal combustion engine is investigated in this chapter by using the geometry equations provided in the *Tribology Handbook* for the computational model. The piston will travel a prescribed distance governed by the following equation for piston position provided in the *Design of Machinery* textbook by Norton [52]:

$$x = r\cos(\omega t) + l\sqrt{1 - \left(\frac{r}{l}\sin(\omega t)\right)^2} \tag{6.1}$$

where r is the crank length measured from the connecting pins centerline axes, l is the link length also measured from the connecting pins centerline axes, ω is the cranks rotational velocity, and t is the time of motion. The use of equation 6.1 will provide piston position after a certain amount of travel time, giving the necessary length dimension for the cylinder.

6.4. Computational Model

The 3D CAD models for the piston, piston rings, and cylinder were developed using the equations provided in the *Tribology Handbook*. A cylinder pressure of 6.9 MN/m^2 was chosen based on the graph illustrated in figure 6.2, from which the dimensions for the piston ring land width, W is provided. Using the graph in figure 6.3, a gudgeon pin wall thickness, t and pin outside diameter, d was selected to ensure that their ratio provided allowable fatigue strength at this cylinder pressure. Thus, the thickness of the pin is chosen to be 1.5 mm and the pin outside diameter will be 10 mm, giving a ratio of 1.5 / 10 = 0.15. The piston ring groove diameters were then calculated using the equations provided in figure 6.4 with the cylinder bore diameter, D selected from figure 6.5. With a cylinder bore diameter chosen to be 100 mm, a diameter of 81.5 mm for the ring grooves at A and a diameter of 80.5 mm for the ring groove at B shown in figure 6.4 were calculated.

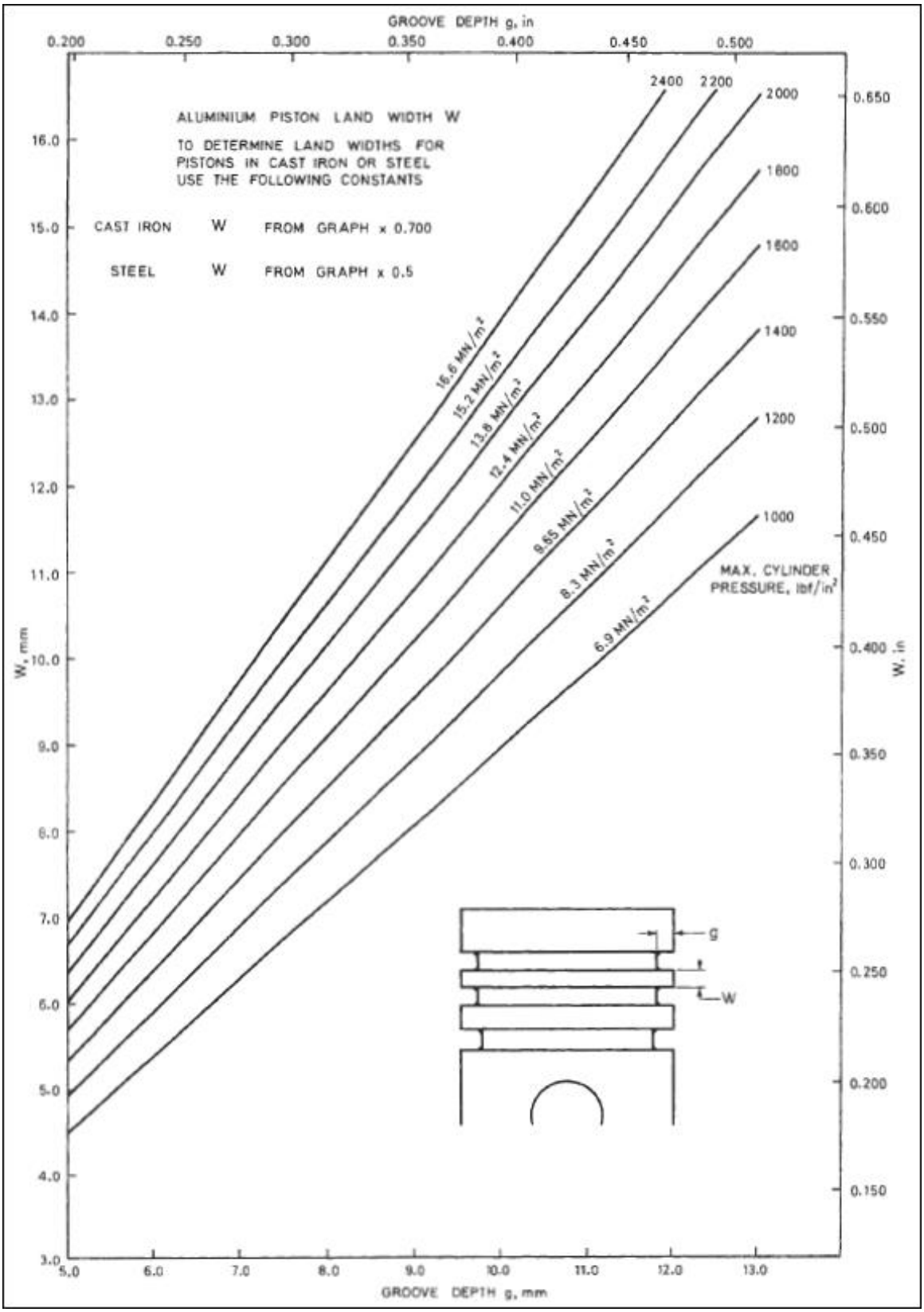

Figure 6.2, Piston Ring Groove Dimensions

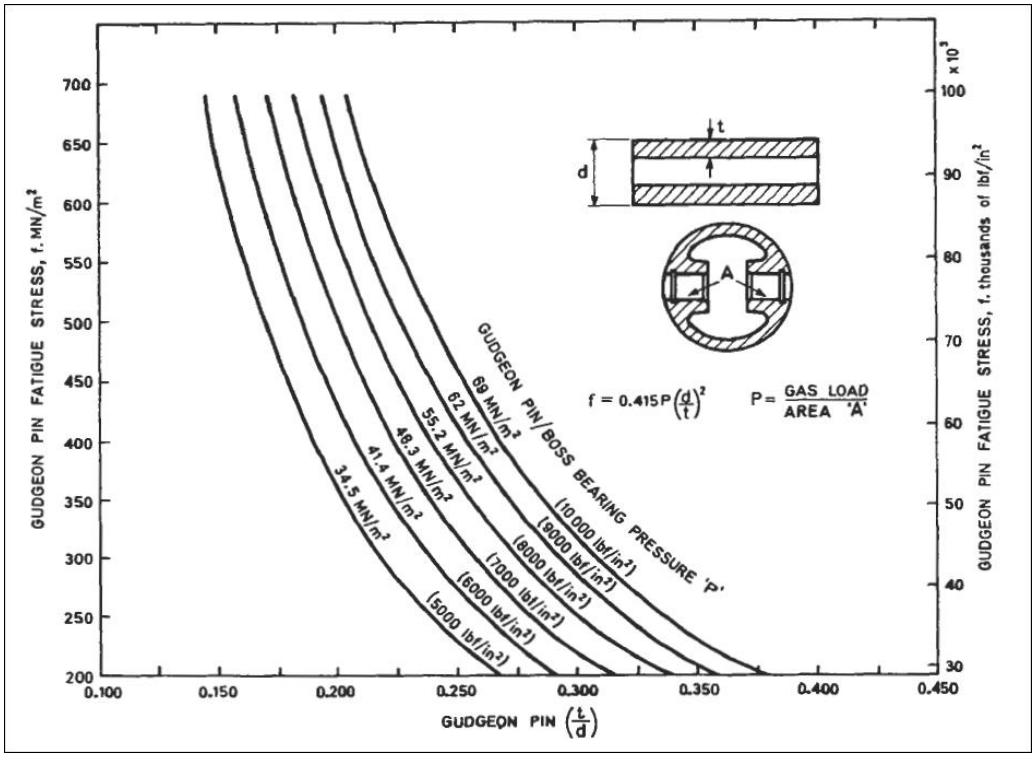

Figure 6.3, Gudgeon Fatigue Strength

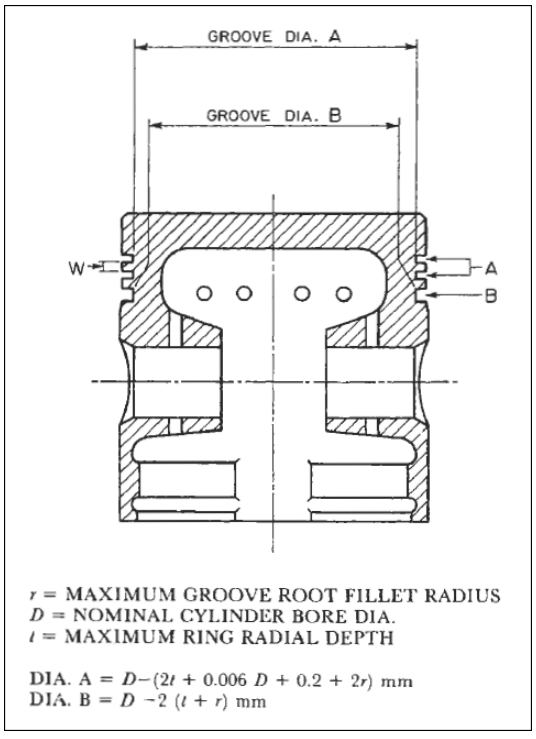

Figure 6.4, Piston Ring Groove Diameter

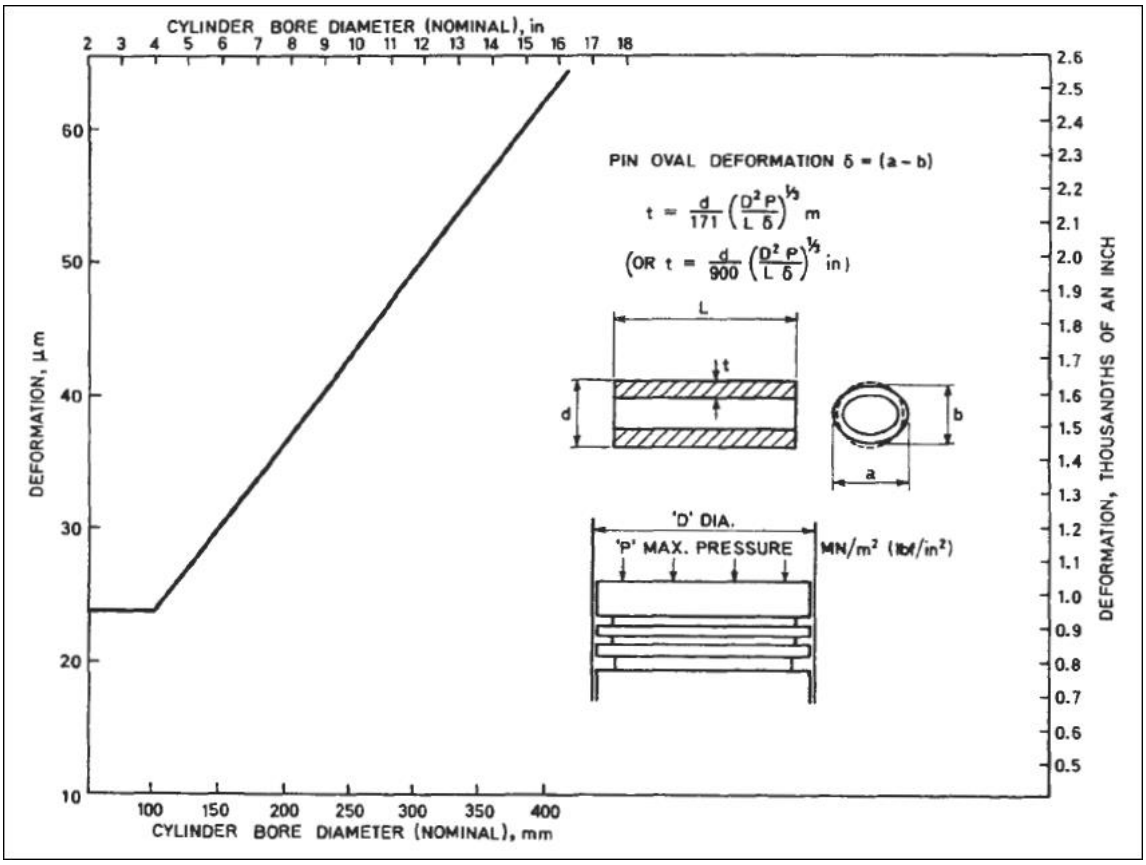

Figure 6.5, Gudgeon Pin Allowable Ovality

The dimensions for the piston rings were then calculated by using the parameters suggested in table 6.1. With a cylinder bore dimeter of 100 mm, the selected axial width for the piston rings, w_r is 10 mm and the radial thickness, t_r is 10 mm. Groove side clearance is also calculated using the equation in table 4, with a side clearance of 0.25 mm calculated. The 3D CAD models for the cylinder, piston, and piston rings are shown in figure 6.6. Choosing a starting crank angle of 75 degrees, the distance of piston travel used for the FEA computation is 28.06 mm as shown in figure 6.7.

Table 6.1, Suggested piston ring dimensions [51]

Suggested sizes of rings				
Units	Cylinder diameter (b)	Piston ring		Groove side clearance, C
		Axial width	Radial thickness	
Millimeters	25-75	3-5	3-6	C = 0.025 x axial width (N.B. - Groove tolerance H7)
	76-150	5-10	5-10	
	151-230	6-12	6-12	
	230-400	10-19	10-19	
	400-800	12-25	12-25	
Inches	1-3	0.125-0.187	0.125-0.218	
	3-6	0.187-0.375	0.187-0.437	
	6-9	0.250-0.500	0.250-0.500	
	9-16	0.375-0.750	0.375-0.750	
	16-30	0.500-1.000	0.500-1.000	

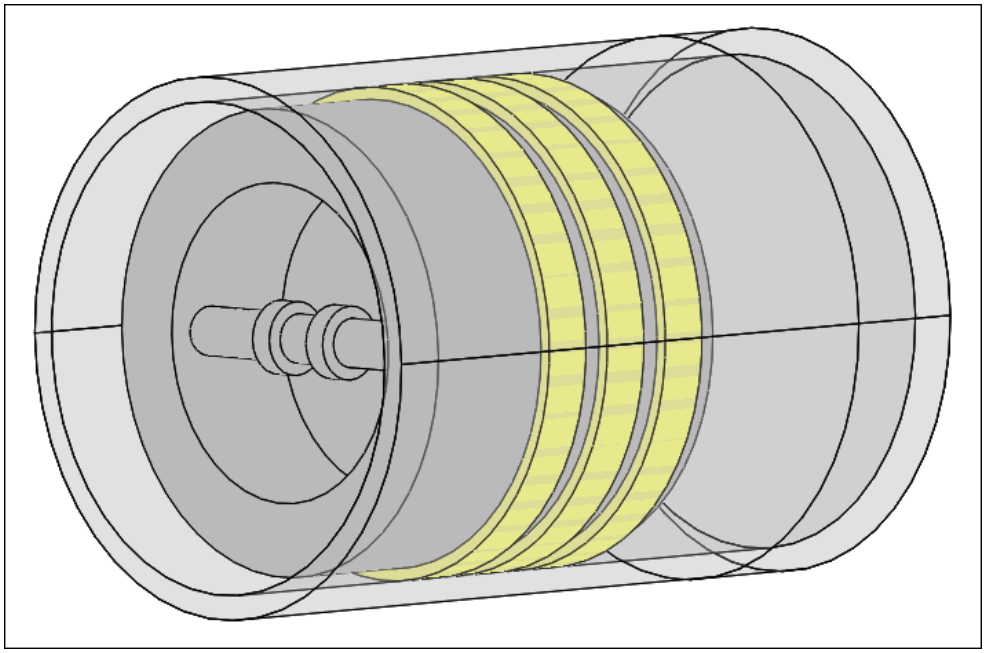

Figure 6.6, Piston, Cylinder, and Piston Ring 3D CAD Models

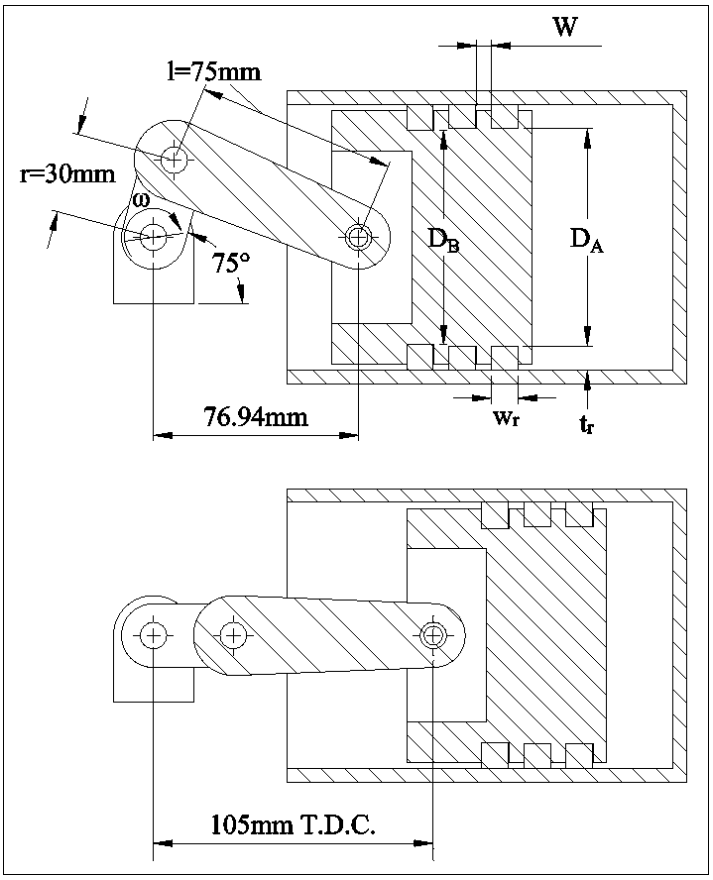

Figure 6.7, Clevis, Crank, And Link Dimensions and Piston Travel Distance to Top Dead Center with an Initial Crank Angle of 75 Degrees from Horizontal

Figure 6.8 shows the FEA computational model used for the piston / cylinder arrangement. The primary area of concern for the transient friction measurement is between the piston rings and cylinder bore so that model simplification is rationalized by only using the piston, piston rings, and cylinder in the calculations. Since translation of the piston is in the direction of top dead center, it is assumed that any gas mixture has already escaped from the cylinder leaving no internal pressure. An ambient pressure of 1 earth atmosphere was applied to the outside of the cylinder. The cylinder is fixed at both ends preventing any rotation or translation of the cylinder body.

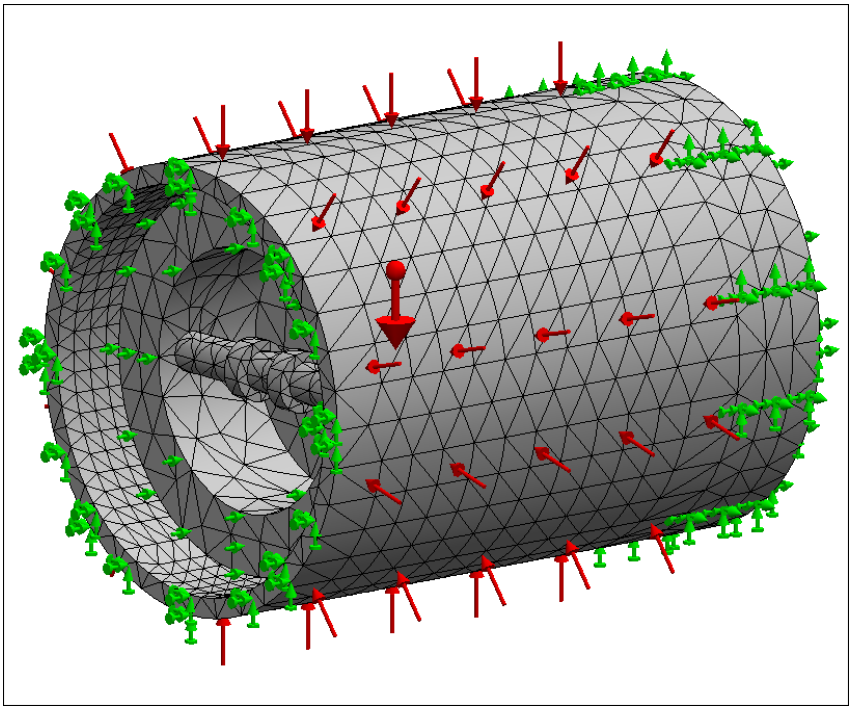

Figure 6.8, Piston / Cylinder Arrangement with Initial Conditions Shown

Linear elastic material properties are used with a modulus of elasticity of 66 GPa, yield strength of 0.250 GPa, and Poisson's ratio of 0.27 defined for the grey cast iron used for the cylinder, piston, and piston rings. There are 15,051 TETRA10 elements in the FEA model with a global mesh size of 10 mm and a 5 mm mesh refinement specified at the outside diameter of the piston rings and the cylinder inside bore diameter. Figure 6.9 shows the contact conditions used in the calculations where the piston rings are bonded to the piston and no penetration contact is defined between their outer diameter and cylinder bore diameter with a value given for the static coefficient of friction, μ_0. Table 6.2 lists the parameters used for three separate FEA calculations with the static coefficient of friction being the only value changed for each load case. Defining μ_0 = 0.95, 0.55, & 0.15 for the three load cases, all other values remain the same and the transient friction response for each load case is plotted in figure 6.10.

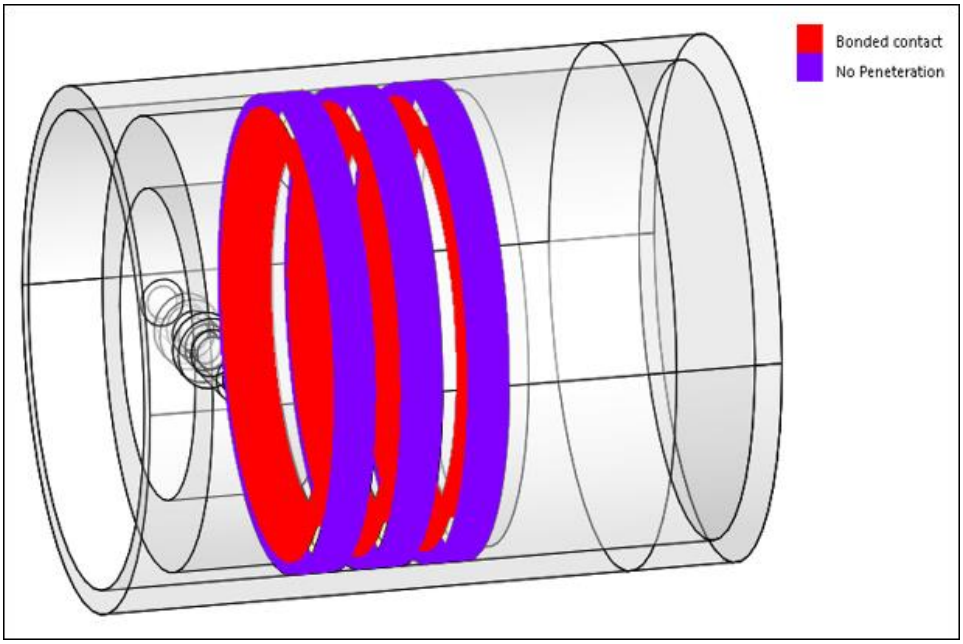

Figure 6.9, Contact Condition Plot for the Piston / Cylinder Arrangement

Table 6.2, Piston / Cylinder Arrangement Simulation Parameters

Piston / cylinder / ring pack simulation parameters		
Parameter	**Value**	**Units**
Nominal cylinder pressure, P	100,000	N/m^2
Nominal cylinder bore diameter, D	100	mm
Gudgeon pin thickness, t	1.5	mm
Gudgeon pin diameter, d	10	mm
Piston ring groove dia. (qty. 2), D_A	81.5	mm
Piston ring groove dia. (qty. 1), D_B	80.5	mm
Piston Ring land width, W	5.6	mm
Piston ring axial width, w_r	10	mm
Piston ring radial thickness, t_r	10	mm
Piston Ring side clearance, C	0.25	mm

To simulate system run-in, a linear displacement time curve is applied to the piston with zero translation at equipment start up and final position reached at 2 seconds. Figure 6.10 shows the position time curve used in the FEA computations.

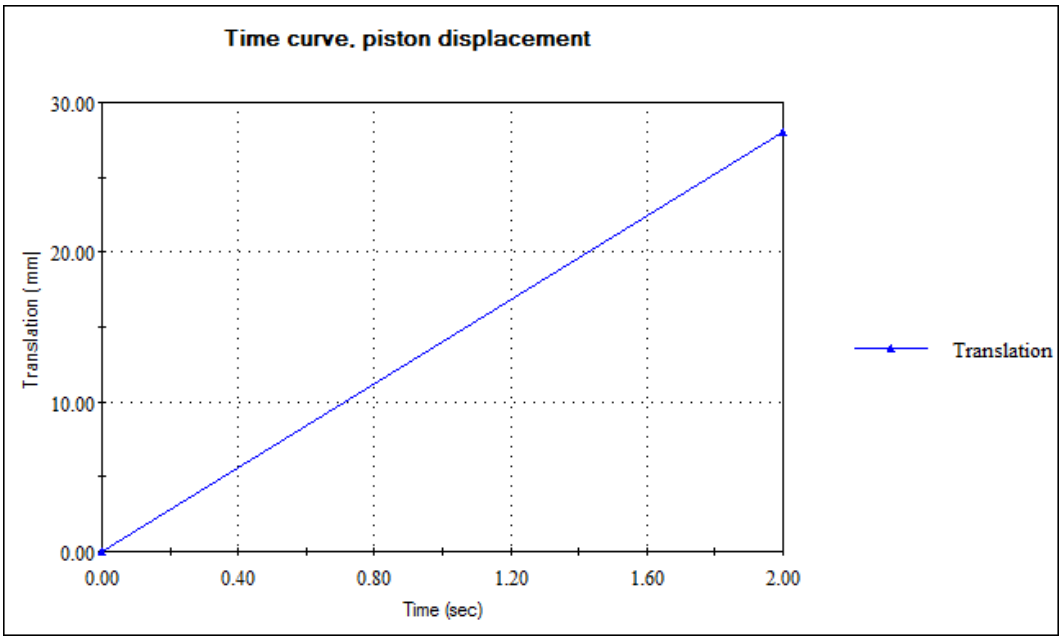

Figure 6.10, Resultant Contact Force at the Piston and Piston Ring Contacting Surface

6.5. Results

Using the initial conditions listed in table 6.2, the transient friction force for the piston / cylinder arrangement is shown in figure 6.11 for three different static coefficient of friction load cases. The contact friction force is measured at the frictional contact interface between the outside diameter of the piston rings and inside cylinder bore radius for the length of time of the solution run. Figures 6.12 and 6.13 show the von Mises stress distribution and contact pressure plots at the final time step (t = 2 sec).

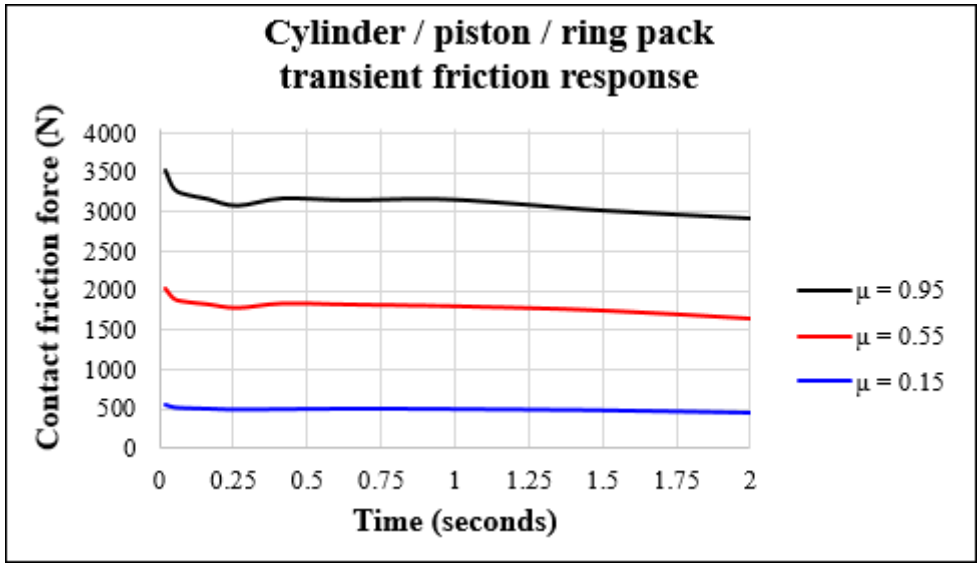

Figure 6.11, Resultant Contact Force at the Piston and Piston Ring Contacting Surface

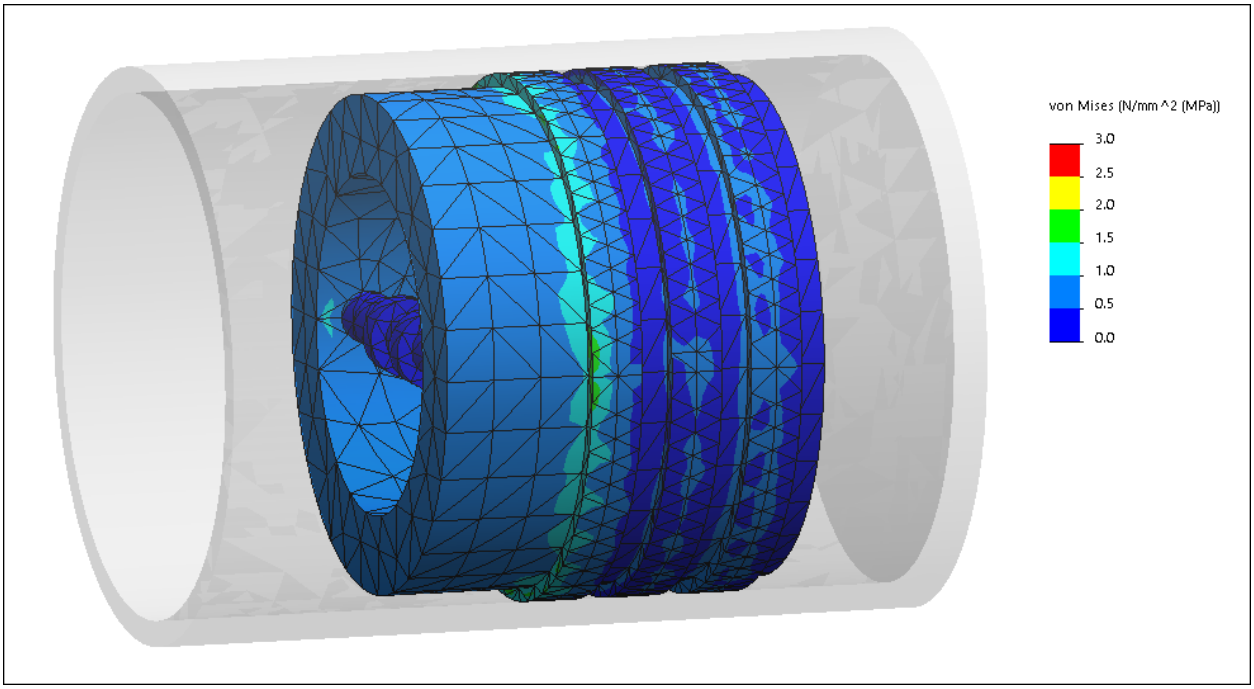

Figure 6.12, von Mises Stress Distribution at Final Time Step, Piston / Cylinder Arrangement, μ=0.95

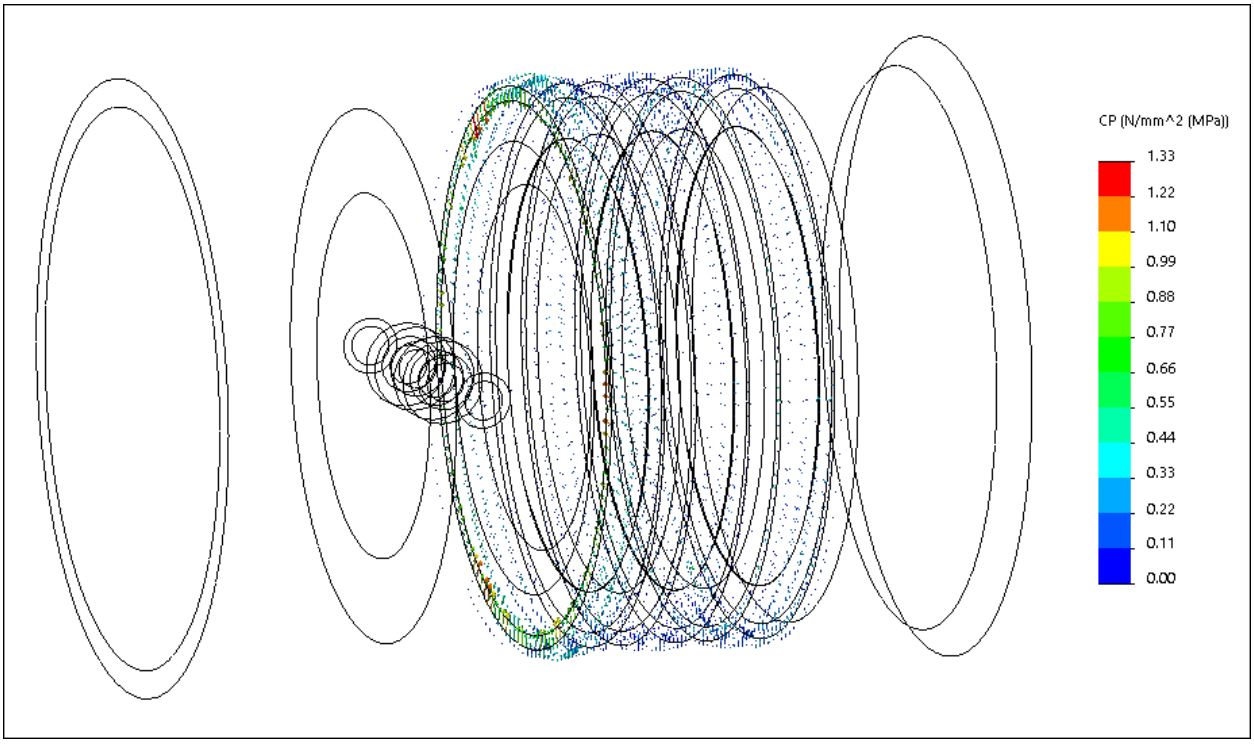

Figure 6.13, Contact Pressure Plot at Final Time Step, Piston / Cylinder Arrangement, μ=0.95

6.6. Conclusion

In figure 6.11 a transient friction response curve for the piston ring / cylinder frictional interface is shown for a total running time of 2 seconds with three different static coefficient of friction values used. As can be seen in the higher friction load case, there is considerable friction action in the beginning stages of motion with a rapid drop of 500 N in frictional force. This sudden drop in friction could lead to slip motion or jerk phenomenon in the systems components and thus reducing the static coefficient of friction as in the other 2 load cases shows that a more level start up friction can be achieved.

7. Conclusions

7.1. Summary of results

In this thesis, the transient frictional response during run-in for several tribo-mechanical systems was investigated. After an introduction into the science of tribology and a discussion about its history, theoretical predictions for fluid self-organization at wetted frictional interfaces during run-in is presented. It was shown that by providing an optimal hydrodynamic roughness-fluid interface, the friction and wear is minimized and always seeks an equilibrium value. It is hoped that the mathematical framework for calculating optimal friction and wear at specific lubricities will motivate future experimentation into fluid-self organization phenomenon.

Next, the transient frictional response of three commonly used tribo-mechanical systems during run-in were analyzed using FEA computations. It was shown that a high static coefficient of friction value yields a highly active transient friction response for these systems. By adjustment of this friction coefficient, a more stabilized friction response may be obtained more rapidly which may lead to more optimized and shorter run-in schedules for new equipment.

The lower limit for the static coefficient of friction of 0.15 was chosen to use in the FEA computations since this value is typical for dry lubricants such as graphite or molybdenum disulfide (MoS_2) [3]. By using this value for the coefficient of friction, the FEA results show that the transient friction response rapidly stabilizes during run-in and thus using these types of additives in metal matrix composites in interfacing components will most likely shorten the required run-in schedule for new equipment. In order to simulate very rough surfaces, a static coefficient of friction value of 0.95 was chosen and it is shown in the FEA results that this high value in friction results in a highly active transient friction response. A friction coefficient of 0.55 was then used to simulate medium rough surfaces and it was shown in all three tribo-

mechanical systems that this value does not improve the transient friction response very much when compared with the uppermost coefficient value.

Using dry lubricants such as graphite is a common approach used to reduce friction when the use of liquid lubricants is unfeasible. A low cost means for using graphite as a lubricant on interacting frictional surfaces is available by means of cementing a strip of graphite-reinforced material onto the working surfaces [53]. The advantage of this approach is that once the layer of graphite has reached failure, the composite strip can be removed and a new layer applied.

Another promising material for reduction in friction and wear not commonly discussed in the literature is graphene due to its extremely high strength capacity as well as its high degree of impermeability, reducing oxidation development [54]. Most research in using graphene at the nano and micro scales has indicated that its use as a lubricant at the macro-scale will yield very good friction and wear characteristics with a huge reduction in coefficient of friction values, dropping from 0.9 – 1.0 for regular steel to 0.15 – 0.16 for graphene coated steel.

7.2. Future Work

Given the opportunity to present a research poster with the results for the three tribo-mechanical systems investigated in this thesis at the 2016 STLE Frontiers conference in Chicago on November 13th through the 15th, I was able to have many interesting discussions with the judges and conference attendees regarding potential future research in the area of tribo-mechanical run-in.

One of the topics that came up was to apply surface asperity geometric detail in the FEA models. By applying statistical surface asperity modeling such as the Greenwood and Williamson statistical contact model [55], or the more complicated friction hardening FEA contact model proposed by Buczkowski and Kleiber [56], a higher degree of fidelity in the modeling of transient frictional run-in with surface asperity plastic deformation can be investigated.

Another topic discussed was to implement computational fluid dynamics (CFD) modeling so that boundary lubrication with lubricating fluids can be explored. This area of computational transient modeling incorporating the boundary lubrication regime during run-in would further constitute my motivation for future research into the fluid self-organization effects discussed in chapter three.

It would also be interesting to investigate graphene's tribological properties further at the macro-scale. Since graphene has extremely high strength properties, the interest would be to investigate graphene's effect on the reduction in friction and wear when compared with graphite. Furthermore, the question could also be asked about lattice direction of the graphene and its influence on tribological properties.

References

[1] E. Rabinowicz, *Friction and Wear of Materials*: Wiley, pp. 65-69, 1995.

[2] "Introduction To Tribology", STLE, [Online]. Available: http://www.stle.org/files/What_is_tribology/Tribology.aspx [Accessed 16 November 2016].

[3] B. Bhushan, *Introduction to Tribology*: Wiley, pp. 207-229 & 255, 2013.

[4] A. Z. Szeri, *Tribology: Friction, Lubrication, and Wear*: Taylor & Francis Group, pp. 2, 60, 1980.

[5] T. A. Stolarski, *Tribology in Machine Design*: Butterworth-Heinemann, pp. 6-12, 1990.

[6] I. M. Hutchings, "Leonardo da Vinci′s studies of friction," *Wear*, vol. 360–361, pp. 51-66, August 2016.

[7] S. Seireg, *Friction and Lubrication in Mechanical Design*: CRC Press, p. 7, 1998.

[8] D. Dowson, *History of Tribology*: Wiley, pp. 160-165, 1998.

[9] S. R. Schmid, B. J. Hamrock, and B. O. Jacobson, *Fundamentals of Machine Elements, Second Edition*: Taylor & Francis, pp. 353-357, 2006.

[10] D. F. Moore and D. W. Hopkins, *Principles and Applications of Tribology: Pergamon International Library of Science, Technology, Engineering and Social Studies: International Series in Materials Science and Technology*: Elsevier Science, p. 376, 1975.

[11] K. C. Ludema, *Friction, Wear, Lubrication: A Textbook in Tribology*: CRC Press, p. 98, 1996.

[12] I. Newton, *The Principia*. Trans. Andrew Moore. New York, NY: Prometheus Books, pp. 223-227, 1995.

[13] T. Mang, *Encyclopedia of Lubricants and Lubrication*: Springer Berlin Heidelberg, p. 1999, 2014.

[14] B. Armstrong-Hélouvry, *Control of Machines with Friction*: Springer US, p. 15, 1991.

[15] K. Nisbett and R. Budynas, *Shigley's Mechanical Engineering Design, Eighth Edition*: McGraw-Hill Education, pp. 598-599, 2008.

[16] ASM International, *ASM Handbook: Friction, Lubrication, and Wear Technology. Vol. 18*: ASM International, pp. 1802-1803, 1992.

[17] C. Bernardin, DeMarco, et. al. 2016 [Online], *Maple Programming Guide*. Available: http://www.maplesoft.com/documentation_center/maple2016/ProgrammingGuide.pdf [Accessed 11 December 2016].

[18] M. Lombard, *Solidworks 2013 Bible*: Wiley, 2013.

[19] Solidworks, [Online], *SolidWorks Simulation Hands-on Test Drive*. Available: http://www.solidworks.com/sw/docs/edu_simulation_hotd_instructor_2013.pdf [Accessed 11 December 2016].

[20] K. H. Huebner, *The Finite Element Method for Engineers, Third Edition*: Wiley, p. 437, 1995.

[21] L. N. Trefethen, *Finite Difference and Spectral Methods for Ordinary and Partial Differential Equations, Chapter 4: Accuracy, Stability, and Convergence*: unpublished text [Online], Available: http://people.maths.ox.ac.uk/trefethen/pdetext.html [Accessed 29 October 2016].

[22] D. Dowson, C. M. Taylor, and M. Godet, *The Running-In Process in Tribology: Proceeding of the 8th Leeds–Lyon Symposium on Tribology, Held in the Institute National des Science Appliquées de Lyon, France, 8–11 September 1981*: Elsevier Science, p. 25, 2013.

[23] P. Kumar C, P. L. Menezes, and S. V. Kailas, "Role of Surface Texture on Friction under Boundary Lubricated Conditions," *Tribology Online,* vol. 3, pp. 12-18, 2008.

[24] P. L. Menezes, Kishore, and S. V. Kailas, "Influence of surface texture and roughness parameters on friction and transfer layer formation during sliding of aluminium pin on steel plate," *Wear*, vol. 267, pp. 1534-1549, September 2009.

[25] V. Mortazavi, C. Wang, and M. Nosonovsky, "Stability of frictional sliding with the coefficient of friction depended on the temperature," *Journal of Tribology*, vol. 134, p. 041601, 2012.

[26] M. Nosonovsky, Mortazavi, V., Wang, C. *Thermodynamic Approach To Coulomb Friction, Wear, And Self-Lubrication:* STLE Conference, 2010.

[27] R. G. Bayer, "Fundamentals of wear failures," *Materials Park, OH: ASM International, 2002.*, pp. 901-905, 2002.

[28] K. G. Budinski, *Friction, wear, and erosion atlas*: CRC Press, 2013.

[29] Y. Cengel and J. Cimbala, *Fluid Mechanics Fundamentals and Applications: Third Edition*: McGraw-Hill Higher Education, pp. 58-59, 2013.

[30] T. Røn and S. Lee, "Influence of temperature on the frictional properties of water-lubricated surfaces," *Lubricants*, vol. 2, pp. 177-192, 2014.

[31] V. Mortazavi. (2014). *Modeling of Instabilities and Self-organization at the Frictional Interface (Doctoral dissertation).* Available: http://dc.uwm.edu/cgi/viewcontent.cgi?article=1539&context=etd [Accessed 12 November 2016].

[32] B. Bhushan, *Modern Tribology Handbook, Two Volume Set, Chapter 13: Friction And Waer Measurement Techniques*: CRC Press, 2000.

[33] C. Seyfert, "Tribometers, Rotational, for Sliding Wear and Friction," *Encyclopedia of Lubricants and Lubrication*, pp. 2138-2155, 2014.

[34] R. L. Fusaro and L. R. Center, *How to Evaluate Solid Lubricant Films Using a Pin-on-disk Tribometer*: National Aeronautics and Space Administration, Lewis Research Center, pp. 1-3, 1986.

[35] P. J. Blau, *Friction and wear transitions of materials*: Noyes Publications, pp. 170-196, 1989.

[36] M. Nosonovsky and V. Mortazavi, *Friction-Induced Vibrations and Self-Organization: Mechanics and Non-Equilibrium Thermodynamics of Sliding Contact*: CRC Press, p. 68, 2013.

[37] "Static Coefficient of Friction Measurement Using Tribometer", Nanovea, [Online], Available: http://nanovea.com/App-Notes/static-friction-measurement.pdf [Accessed 31 October 2016].

[38] A. Standard, "G99, Standard test method for wear testing with a pin-on-disk apparatus," *ASTM International, West Conshohocken, PA*, 2006.

[39] "Pin-On-Disk (CSM Instruments)", NTNU, [Online], Available: https://www.ntnu.edu/ipm/tribology-lab/pin-on-disk [Accessed 31 October 2016].

[40] M. A. Kabir, Higgs, C. F., Lovell, M. R., "A Pin-on-Disk Experimental Study on a Green Particulate-Fluid Lubricant," *Journal of Tribology*, vol. 130, pp.1-6, 2008.

[41] E. Oberg, F. D. Jones, H. L. Horton, H. H. Ryffel, and J. H. Geronimo, *Machinery's handbook, 27th Edition* : Industrial Press New York, pp. 2230-2235, 2004.

[42] G. Stachowiak and A. W. Batchelor, *Engineering Tribology, Second Edition*: Elsevier Science, p. 146, 2013.

[43] V. Curcio, *Chrysler: The Life and Times of an Automotive Genius*: Oxford University Press, 2001.

[44] A. Harnoy, *Bearing Design in Machinery: Engineering Tribology and Lubrication*: Taylor & Francis, p. 22, 2002.

[45] McMaster-Carr. (2016). *Food-Grade Oil-Embedded Sleeve Bearings*. Available: https://www.mcmaster.com/#food-grade-bushings/=1546cpi [Accessed 17 October 2016].

[46] M. Lamantia, "Re: Food Grade Bearings Used In The Food Industry." Message to Morien, R., 17 October 2016. E-mail.

[47] E. Hahlbeck, "Re: Journal Bearing Friction Resonse." Message to Morien, R., 12 October 2016. E-mail.

[48] igus. (2016). *iglide® 2016 Complete Catalog*, [Online], Available: http://www.igus.com/contentData/Product_Files/Download/pdf/2016%20iglide%20catalog%20complete.pdf [Accessed 17 October 2016].

[49] S. Marx and R. Junghans, "Friction and wear of highly stressed thermoplastic bearings under dry sliding conditions," *Wear*, vol. 193, pp. 253-260, 1996.

[50] J. Moran and T. Sucharitakul, "Variations in Dry Sliding Friction Coefficients with Velocity," *Recent Advances on Mechanics, Materials, Mechanical Engineering and Chemical Engineering, 2015 INASE Conference*, 2015.

[51] M. J. Neale, *The Tribology Handbook*: Elsevier Science, pp. A30-A32, 1973.

[52] R. L. Norton, *Design of Machinery, An Introduction To The Synthesis And Analysis Of Mechanisms And Machines, Fourth Edition:* McGraw-Hill., pp. 650-663, 2008.

[53] C. Berg, S. Batra, and J. Tirosh, "Friction and wear of graphite fiber composites," *Journal of Research*, vol. 76, pp. 41-52, 1972.

[54] D. Berman, A. Erdemir, and A. V. Sumant, "Graphene: a new emerging lubricant," *Materials Today*, vol. 17, pp. 31-42, 2014.

[55] J. Greenwood and J. Williamson, "Contact of nominally flat surfaces," in *Proceedings of the Royal Society of London A: Mathematical, Physical and Engineering Sciences*, 1966, pp. 300-319.

[56] R. Buczkowski and M. Kleiber, "Statistical models of rough surfaces for finite element 3D-contact analysis," *Archives of Computational Methods in Engineering,* vol. 16, pp. 399-424, 2009.